UNIVERSIDAD DE CONCEPCIÓN
FACULTAD DE CIENCIAS FÍSICAS Y MATEMÁTICAS

STACKING IN THE ALMA LENSING CLUSTER SURVEY FIELDS

Tesis presentada a la Facultad de Ciencias Físicas y Matemáticas de la Universidad de Concepción para optar al grado académico de Magíster en Ciencias con Mención en Física

Por: Andrea Paz Guerrero Pérez

Profesor Guía: Neil Nagar

Noviembre 2021
Concepción, Chile

AGRADECIMIENTOS

Agradezco a mi familia, amigos y pareja por su apoyo y amor incondicional, por hacer mis días más amenos y por siempre darme palabras de aliento cuando lo necesito.

Agradezco también a mi supervisor Neil Nagar, por el increíble apoyo en esta tesis, por sus sabios consejos y confianza en mis conocimientos.

Agradezco a la colaboración de ALCS por sus muy útiles comentarios que contribuyeron a hacer mejor esta tesis.

Finalmente, me gustaría agradecer el apoyo financiero de parte de la Agencia Nacional de Investigación y Desarrollo (ANID, Chile) / Programa Formación de Capital Humano Avanzado (PFCHA) / Magíster Nacional/2019 - 22191646, Nucleo Milenio TITANs (NCN19−058), Basal AFB-170002 y Dirección de Postgrado, ya que fueron parte fundamental del desarrollo de esta investigación.

Resumen

En esta tesis presentamos dos nuevos softwares de stacking, uno de stacking del continuo y otro de stacking de espectros, que pueden usarse independiente o como una tarea del software Common Astronomy Software Applications package (CASA). Estos softwares fueron usados para realizar un análisis de stacking en las observaciones del ALMA Lensing Cluster Survey (ALCS). El survey ALCS observó (en el submilimétrico) 33 cúmulos de galaxias masivos en el submilimétrico a redshifts intermedios ($0.2 < z < 0.9$), que han sido previamente estudiados en observaciones ópticas e infrarrojas, por lo que ofrece un set de datos prometedor para stacking.

Realizamos el stacking del continuo observado en 1.2mm para ∼1400 galaxias de cúmulo y ∼1900 galaxias de campo (individualmente no-detectadas), sobre tres rangos de redshift y de masa estelar (z = 0–1.0 para galaxias de cúmulo y z = 0–1.6 para galaxias de campo, y $M_*[M_\odot]$ =10^9–4.6×10^{11}).

Con detecciones encontradas en el stack de continuo derivamos el promedio de masas de polvo, masas de gas y tasas de formación estelar, comparando resultados entre galaxias de cúmulo y de campo, en función de su masa estelar y redshift. También derivamos el contenido promedio de gas molecular con stacking espectral de galaxias seleccionadas de acuerdo a sus tasas de formación estelar.

A partir del stacking del continuo encontramos que tanto las galaxias del cúmulo como las de campo presentan valores bajos de masas de gas, fracción de polvo, tasas de formación estelar al compararlas con resultados de galaxias individualmente detectadas. Para galaxias de campo y cúmulo de la misma masa estelar, encontramos que las de campo muestran valores más cercanos al esperado para galaxias de la secuencia principal, que las de cúmulo. Además, la diferencia entre los valores para galaxias de secuencia principal y nuestras galaxias, disminuye con menor redshift. En las tasas de formación estelar obscurecidas (de ALMA) suelen ser más bajas que las tasas no-obscurecidas (de observaciones ópticas/infrarrojas).

A partir del stacking de espectros, encontramos una potencial detección de la línea CO J:4-3 (con señal a ruido ~ 4), al combinar galaxias con las tasas de formación más altas.

Estos resultados nos otorgan una mirada importante a las propiedades reales

galaxias de cúmulo y de campo.

Keywords – galaxies: star formation – galaxies: evolution – submillimeter: galaxies – radio continuum: galaxies – radio lines: galaxies

Abstract

In this thesis we develop and present two novel stacking softwares, for continuum and spectral stacking, that can be used as a standalone Python script or as a Common Astronomy Software Applications package (CASA) task. These softwares were used to perform stacking analysis in the ALMA Lensing Cluster Survey (ALCS). The ALCS observed 33 massive galaxy clusters at intermediate redshifts ($0.2 < z < 0.9$) , previously studied by optical and IR observations, offering a promising dataset for stacking.

We stacked the observed 1.2mm continuum of (individually undetected) ∼1400 cluster and ∼1900 galaxies, over three redshift and three stellar mass bins (over z = 0–1.6 and log $M_*[M_\odot]$ =9–11.7). With stacked 1.2mm continuum detections we were able to derive average dust masses, gas masses and star formation rates. This allowed us to contrast the properties of cluster and field galaxies, and their evolution with stellar mass and redshift. We also derive the average molecular gas content by stacking the emission line spectra in mass- and SFR-selected sub-samples.

From continuum stacking we find lower values of ISM mass fractions, dust mass fractions, SFR and sSFR for both cluster and field galaxies, when comparing to previous results from individually detected galaxies. For field and cluster galaxies in the same stellar mass bin, the former show values closer to the expected Main Sequence (MS) of star-forming galaxies when compared to the latter. Further, the difference between our stacked values and the expected MS increases with decreasing redshift. The ALMA-traced average 'obscured' SFRs are typically lower than the 'unobscured' SFRs obtained from optical to near-IR spectral analysis.

From spectral stacking we find a potential CO J:(4-3) line emission (SNR $\sim$ 4) when stacking galaxies with the highest SFRs.

Our pilot stacking results already provide constraints on the true average properties of cluster and field galaxies.

Keywords – galaxies: star formation – galaxies: evolution – submillimeter: galaxies – radio continuum: galaxies – radio lines: galaxies

Contents

List of Tables

List of Figures

Chapter 1

Introduction

1.1 Galaxy evolution

Understanding how gas reservoirs and star formation rates (SFR) change with stellar mass and environment density, and evolve over cosmic time, is crucial to understand galaxy evolution. Since millimeter (mm) and submillimeter (sub-mm) observations can directly (e.g., via the CO rotational transitions) and indirectly (the sub-mm continuum) trace the gas reservoir and also the SFR (e.g., Carilli and Walter, 2013; Scoville, 2013; Scoville et al., 2014, 2016; Chen et al., 2017; Villanueva et al., 2017; Magnelli et al., 2020; Suzuki et al., 2021), the Atacama Large Millimeter/submillimeter Array (ALMA) is a powerful tool in this area. Most ALMA results thus far come from individually detected galaxies.

As an example, Fig. 1.1.1 shows the ALMA observations of the detected dust 870μm continuum and the detected CO J:3-2 line of a submillimeter galaxy at z=2.12, from Chen et al. (2017).

The mm and sub-mm continuum traces the optically-thin Rayleigh-Jean tail of dust emission (for typical dust temperatures of ∼18–50 K). The conversion of sub-mm flux into dust mass assumes grey-body dust emission with two parameters: the dust emissivity index β (in the Raleigh-Jeans limit the grey-body flux varies as $S_\nu \propto \nu^{2+\beta}$) and the dust temperature T. Typical values of β include $\beta = 1.5 - 2$ for local galaxies and $\beta = 1.2$ to 1.8 for high redshift galaxies (Scoville et al. 2014). Alternatively, the sub-mm flux can be used to estimate the infrared luminosity (e.g., Orellana et al. 2017), and thus SFR, though this conversion is more uncertain

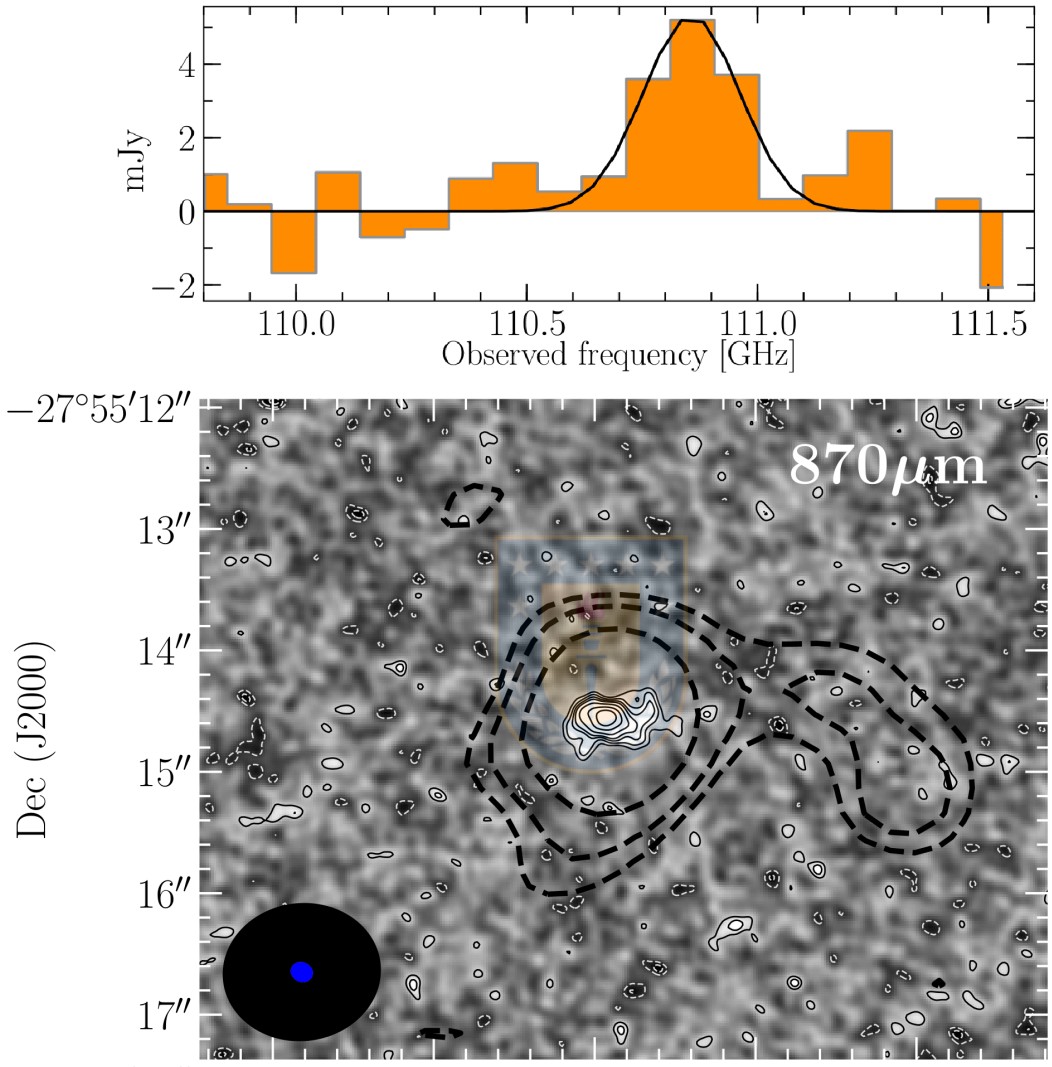

Figure 1.1.1: ALMA observations of a submillimeter galaxy at z=2.12 from Chen et al. (2017). The top panel shows the detected CO J:3-2 line spectrum, observed in 3mm channel maps. The black solid line shows the best fitted Gaussian profile. The bottom panel shows the 870μm continuum map of the dust continuum emission, in which it is possible to see a 10σ detection. Solid contours show different levels of σ, and dotted contours show previous detections described in Hodge et al. (2013). The bottom-left corner shows the synthesized beam for both observations, where the blue one corresponds to the $\sim 0.2''$ of Chen et al. (2017), and the black one corresponds to the $\sim 1''$ from Hodge et al. (2013).

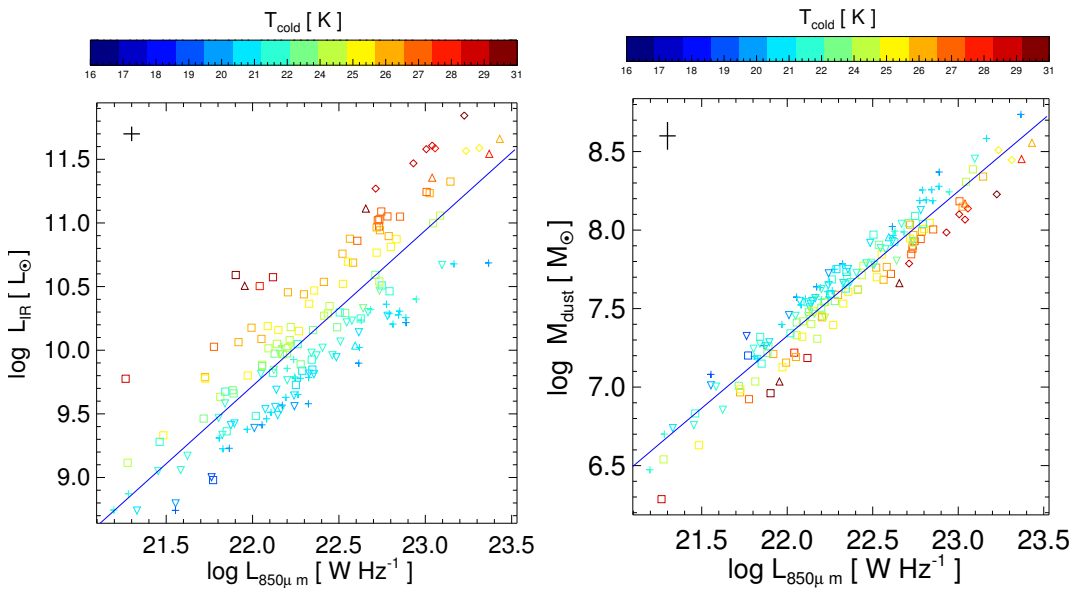

Figure 1.1.2: Dependence of IR luminosity (left panel) and dust masses (right panel) with the 850μm luminosity. The cold dust temperature dependence is shown by the colors and the best fit with the blue line. Symbols show starburst, passive and main sequence galaxies as diamonds, crosses and squares, respectively. The errorbar for each point is shown at the left top corner of each panel with a black cross. Figures from Orellana et al. (2017).

than the previously mentioned conversions to dust and ISM masses, since it is more sensitive to the assumptions of dust temperature(s) and βs.

Fig. 1.1.2 shows the relationship between IR luminosity and dust mass as a function of the submm luminosity at 850μm. Each relationship shows a scatter that depends on the assumed temperature for the cold dust.

Star formation rates and stellar masses of galaxy populations at different redshifts help constrain the evolution of the main sequence (MS) of star formation, i.e. the dependence of SFR on stellar mass (M_*). At a given redshift, higher stellar mass galaxies in the MS have higher star-formation rates, and the median ratio of SFR to stellar mass (the star formation efficiency, or SFE) of MS galaxies increases with redshift (e.g. Elbaz et al. 2011, Rodighiero et al. 2011,Speagle et al. 2014). The main sequence helps to distinguish between galaxies that form more stars than most galaxies, i.e. starburst galaxies that fall above the main sequence, and between galaxies that form less stars than most galaxies, i.e. passive galaxies that fall below the main sequence.

The specific star formation rate (ssfr; SFR/M_*) as a function of redshift and

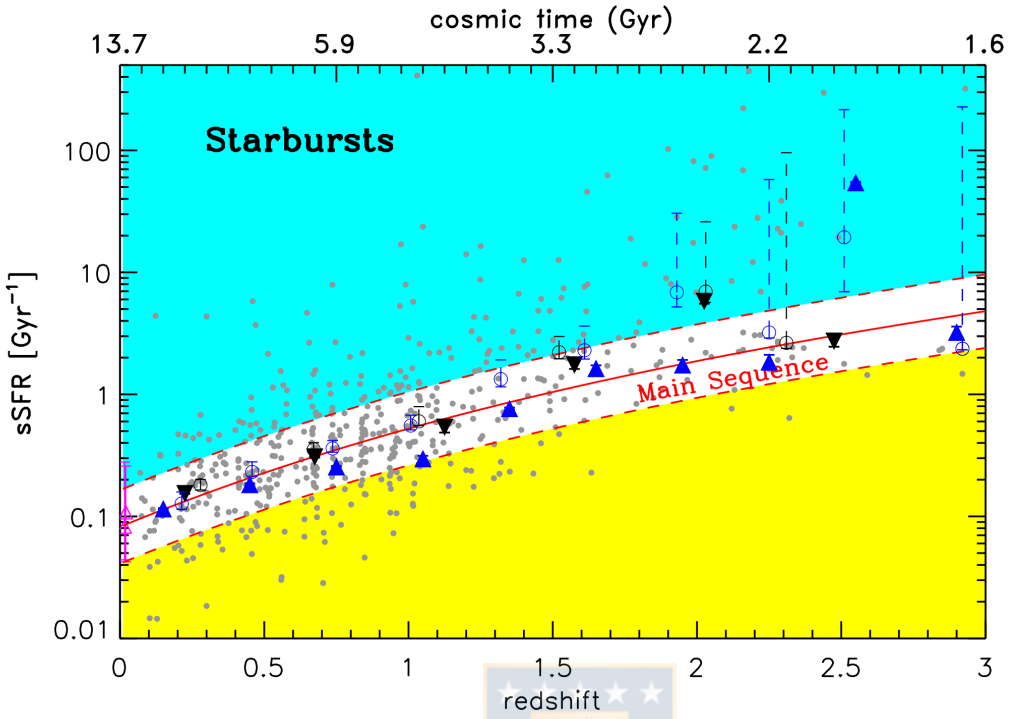

Figure 1.1.3: Median specific star formation rate as a function of redshift and cosmic time for star-forming galaxies. Grey circles show the show individually detected galaxies from GOODS-Herschel. Open circles show the median values of sSFR for GOODS-N (blue) and for GOODS-S (black). Filled triangles show sSFR estimations from detected and undetected stacked galaxies, of GOODS-N (blue upward) and GOODS-S (black downward). The main sequence trend is shown as the red solid line, with the dashed lines showing a factor 2 above and below the best fit. The cyan region distinguishes starburst galaxies as the ones with sSFR $>$ 2$\times$sSFR$_{\rm MS}$, while the yellow regions shows galaxies with lower sSFR. Figure from Elbaz et al. (2011).

cosmic time, from Elbaz et al. (2011), is shown in Fig. 1.1.3. In this case, the best fit to the main sequence is described by,

$$sSFR_{\rm MS}[{\rm Gyr}^{-1}] = 26 \times {\rm t}_{\rm cosmic}^{-2.2} \tag{1.1.1}$$

where t is the cosmic time since the Big Bang in Gyr^{-1}.

Galaxies in clusters and in the field show significant differences (e.g. see reviews by Boselli and Gavazzi 2006, Boselli and Gavazzi 2014). At low redshift, cluster galaxies tend to be more massive, older, and more passive. At redshifts $z < 1$ cluster galaxies have lower mean star formation rates for a fixed stellar mass, when

compared to field galaxies at the same redshift (e.g., $0.04 < z < 0.07$ Paccagnella et al. 2016; $0.4 < z < 0.8$ Vulcani et al. 2010). Low redshift cluster galaxies also have lower dust-to-stellar mass ratios than field galaxies (Bianconi et al., 2020, $z \sim 0.2$). Low redshift cluster galaxies typically exhibit lower molecular gas fractions than field galaxies (e.g. Zabel et al. 2019, Morokuma-Matsui et al. 2021), though in some cases they can have a comparable molecular gas content (Cairns et al., 2019). As redshift increases, there is an increase of blue, star-forming and spiral galaxies in clusters (the Butcher-Oemler effect, e.g., Pimbblet, 2003). At redshifts $\gtrsim 1$, mean SFRs increase with environmental density in both groups (e.g. Elbaz et al. 2007) and clusters (e.g. Popesso et al. 2011).

While large-area or deep pencil beam continuum and spectral line surveys from ALMA are increasingly available, each has revealed relatively few individual detections of dust continuum and/or line emission (e.g. Oteo et al. 2016, Walter et al. 2016, González-López et al. 2017, Franco et al. 2018).

An example of this issue can be seen in Fig. 1.1.4. Here it is possible to see how in the ALMA continuum maps only a few detections were found for the cluster Abell 2744.

Following this idea, a promising avenue to better exploit these data is through *stacking* analysis.

1.2 Stacking

Stacking is a method that allows the decrease of noise in a certain set of data. In astronomy, stacking can be use as a tool to increase the signal-to-noise ratio (SNR) of observations. It averages the data of N sources in order to obtain the average value of the stacked sources. If stacking is performed in a group of undetected galaxies, then, it may be possible to obtain a detection in the average signal, that represents an average property of the individually undetected sources. This is important not only to improve the quality of astronomical data, but also, to uncover galaxies that may, otherwise, not be detected. Thus, stacking individually undetected sources better traces the average properties of a population, when there are only few sources that were individually detected. In this case, previous observations are necesary to obtain the positions of galaxies detected in another wavelength, and to perform the stacked in a wavelength where the galaxies are

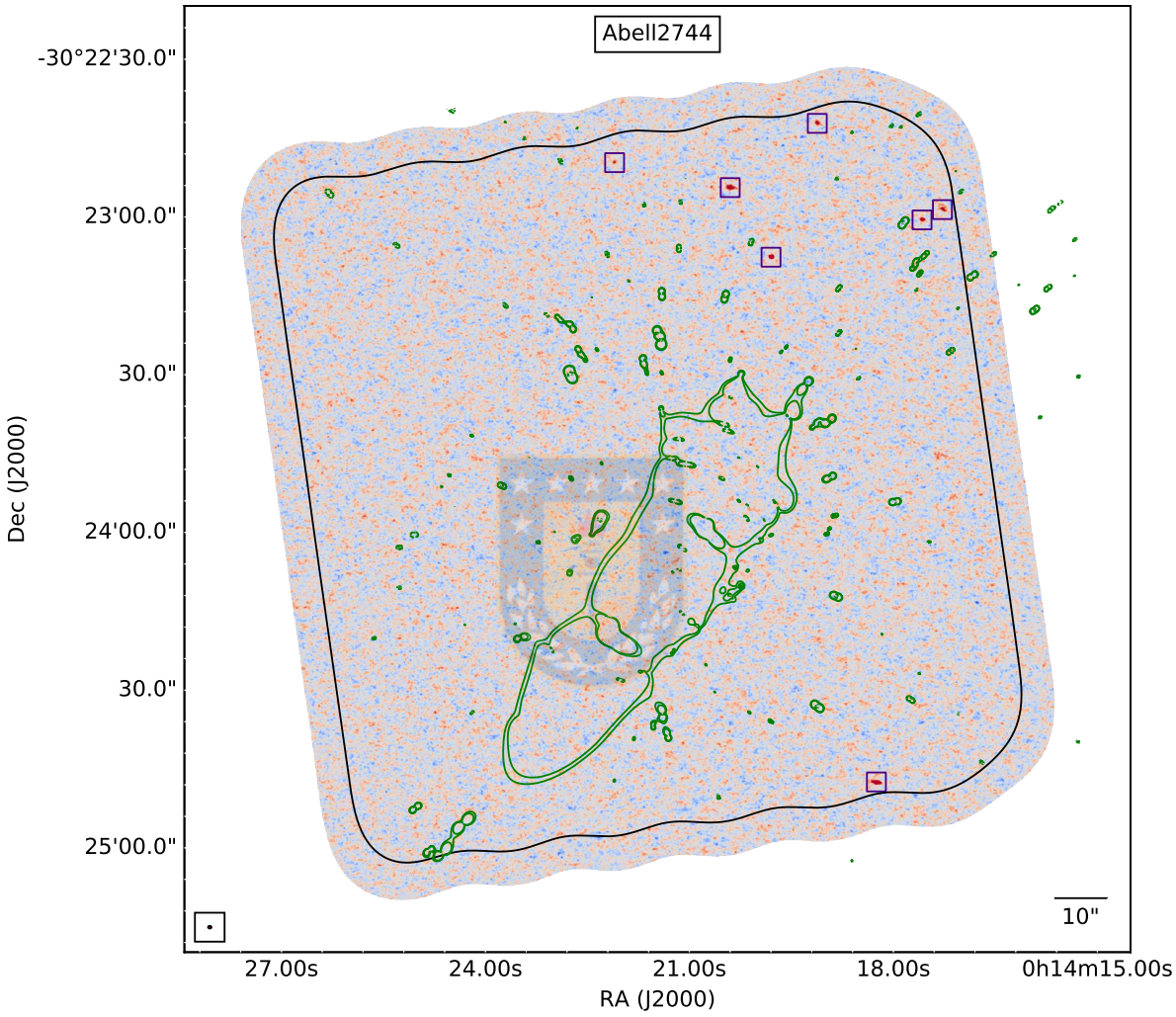

Figure 1.1.4: Submm observations of the Abell 2744 galaxy cluster from González-López et al. (2017)). The 1.1 mm continuum map has a ≈2' × 2' field of view and has a color scale of -5σ to 5σ from blue to red. The continuum detected sources with a S/N $\geq$ 5 are shown with square symbols. The bottom left corner shows the synthesized beam of 0.63"×0.49" and green lines show the highest points of magnification according to their model.

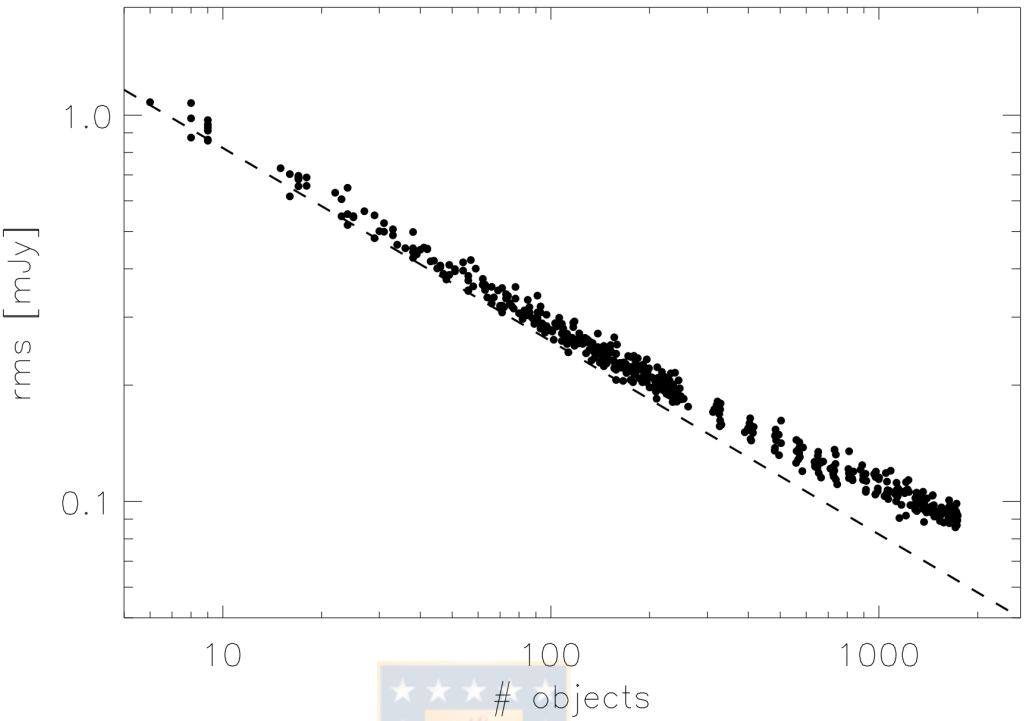

Figure 1.2.1: Noise (rms) of stacked spectra as a function of the number of objects stacked. The black dash line shows the expected decrease of noise by a factor of $\sim \sqrt{N}$. This figure is from Fabello et al. (2011).

not detected.

Stacking works due the uncorrelated nature of the noise in the images. This means that the noise is a random component, that fluctuates between positive and negative values. By combining the images, the positives and negatives can be canceled out, therefore reducing the noise. The noise typically decreases as a factor of $\sim \sqrt{N}$, with N the number of objects stacked. Examples of how the noise decreases can be seen in Fabello et al. 2011 and Delhaize et al. 2013.

Figure 1.2.1 shows the root mean square (rms) noise as a function of numbers of objects stacked, from Fabello et al. (2011).

So far, stacking has proved a powerful tool for different fields, wavelengths ranges and types of data. In extragalactic astronomy for instance, it has helped in the detection of high redshift galaxies (e.g. van Dokkum et al. 2010, Netzer et al. 2016, Maltby et al. 2019, Perger et al. 2019); the creation of stacked composite spectra of a group of galaxies and comparison to synthetic stellar population

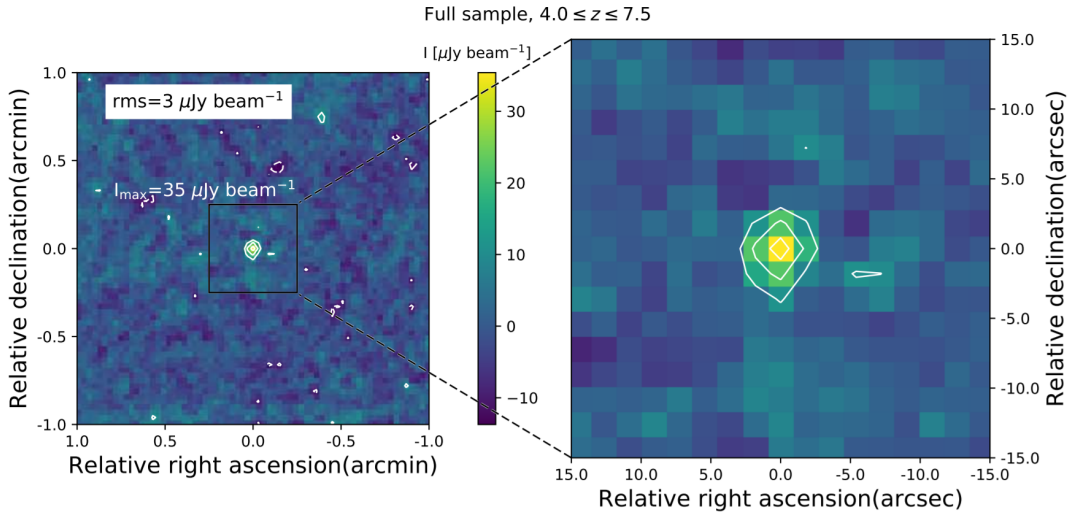

Figure 1.2.2: Median stacked images for radio-non-detected AGN at $4.0 \leq z \leq 7.5$, centered in a 2×2 arcmin^2. The maximum intensity is shown in the center of the image. The right panel shows the inner 30" $\times$ 30" area. Figure from Perger et al. (2019).

models (Cimatti et al. 2008, Domínguez Sánchez et al. 2019) and to increase the depth of already existing surveys (McCracken et al. 2012, Fornasini et al. 2019).

Fig. 1.2.2 shows a stacked detection of high-z individually undetected AGN, from Perger et al. (2019), as an example.

One particular regime that has benefited from stacking is radio astronomy, both due to images and spectra being noisy, and since the signal to noise increases only as $\sqrt{t}$, where t is the observing time.

In interferometry the imaging of the sky is not made directly, but with an array of antennas. The information measured with each pair of antennas in contained in a complex function called "visibility", including amplitude and phase values. Then, the brightness distribution of the sky is obtained with the fast Fourier transform (FTT) of the visibilities. However, there is not infinite number of visibilities to obtain the true brightness distribution of the source (since the number of antennas are limited), which results in extra noise patterns in the observations.

1.3 This work

Recently, a novel ALMA survey, called the ALMA Lensing Cluster Survey (ALCS; P.I. Kotaro Kohno) has completed the observations of 33 massive galaxy clusters, becoming the largest - in area - ALMA surveys targeting galaxy clusters. All clusters have been previously imaged with the Hubble Space Telescope (HST), enabling accurate positions and other quantities derived from HST photometry.

The aim of this thesis is to present new continuum and spectral stacking tools for ALMA images and datacubes, and use these to stack data from the ALCS, thus constraining median dust masses, gas masses, and star formation rates in different redshift and stellar mass bins, and in cluster versus field environments. Given the large survey area, relatively short integration times ($\sim$5 min) per pointing, and the large number of known optical/IR counterparts, this is one of the best existing datasets for a stacking analysis to compare the median properties of cluster and field galaxies.

This thesis is organized as follows: in Section 2 we present the ALCS data and the photometric and spectroscopic catalogs used for our stacking analysis; in Section 3 we describe our methods; in Section 4 we present the results of our stacking analysis, and (sub)mm-derived dust masses, gas masses and SFRs; in Section 5 we discuss and summarize our results.

Throughout the thesis we assume a spatially flat ΛCDM cosmological model with $H_0 = 70$ kms^{-1} Mpc^{-1}, $\Omega_m = 0.7$ and $\Omega_\Lambda = 0.3$.

Chapter 2

Data Description

2.1 Data

This thesis uses data cubes and continuum images from the ALMA Lensing Cluster Survey.

2.1.1 The ALMA Lensing Cluster Survey

The ALMA Lensing Cluster Survey (ALCS; P.I. Kotaro Kohno) is a cycle 6 Large Program of the Atacama Large Millimeter/submillimeter Array (ALMA). The ALCS large program, with over 100 hours of integration, has completed the observations of 33 massive clusters of galaxies at intermediate redshifts, between $0.187 < z < 0.87$ (see Table 2.2.1).

These clusters were selected from previous Hubble Space Telescope (HST) programs, including 5 galaxy clusters from the Hubble Frontier Fields (HFF; Lotz et al. 2017), 12 galaxy clusters from the Cluster Lensing and Supernova Survey with Hubble (CLASH; Postman et al. 2012) and 16 galaxy clusters from the Reionization Lensing Cluster Survey (RELICS; Coe et al. 2019).

The ALMA survey covered a total area of 110 arcmin^2 (primary beam factor cut at 0.5) using a 15-GHz-wide spectral scan and reaching a depth of 70 μJy/beam (1σ) at 1.2 mm. For each cluster an ALMA mosaic was used to cover a region of about $\sim 2 \times 2$ around the core of the cluster. The angular resolution of the observations are $\sim 1 - 1.5''$. The 15-GHz wide spectral scans were used to cover

two frequency ranges of 250.1 - 257.5 GHz and 265.1 - 272.5 GHz. Considering the redshifts of each cluster, the resulting rest-frame spectra include one CO line for the majority of the cluster galaxies, and in some cases the CI line.

In this work, we use dirty maps with a tapered resolution of 2 for continuum stacking, and dirty cubes with 60 km s^{-1} channels and the intrinsic spatial resolution of $\sim 1 - 1.5''$ for spectral stacking.

2.2 Catalogs

In order to perform stacking, both for spectral and continuum stacking, it is necessary to know the exact positions of the galaxies that will enter the stack. Therefore, a compilation of catalogs for each galaxy cluster was made. Since spectral stacking requires accurate positions and redshifts to correctly align stacked emission lines (e.g Maddox et al. 2013, Elson et al. 2019 , Jolly et al. 2020), we have compiled a single ALCS spectroscopic catalog by combining literature spectroscopic redshifts for the 25 clusters with available data, as summarized in Table 2.2.1.

These catalogs include cluster members as well as foreground and background galaxies. Given the relatively low number of available spectroscopic redshifts in each cluster field, and the absence of large spectroscopic catalogs for several clusters, we use photometric catalogs for continuum stacking (since these have accurate positions, and their photometric redshift errors are typically smaller than the redshift bins we use for stacking).

2.2.1 Spectroscopic catalogs

Out of the 33 galaxy clusters from ALCS, 25 clusters have a public spectroscopic catalog available at the moment. Since the stacking includes only undetected galaxies, the galaxies with a detected emission line were removed from the final catalog. Also, it is important to note that the stacking code uses the full catalogs, but that the number of sources that will be used in the stack will be lower, since some galaxies will fall outside the spatial range of the ALCS cubes.

Table 2.2.1: Spectroscopic catalogs for ALCS Clusters

	Cluster	z	References
HFF	Abell 2744	0.308	Richard et al. (2021)
	Abell S1063	0.348	Karman et al. (2017)
			Mercurio et al. (in prep.)
	Abell370	0.375	Richard et al. (2021)
	MACS J0416.10-2403	0.396	Richard et al. (2021)
	MACS J1149.5+2223	0.543	Grillo et al. (2016)
			Treu et al. (2016)
CLASH	Abell383	0.187	Geller et al. (2014)
	Abell209	0.206	Annunziatella et al. (2016)
	RXJ2129.7+0005	0.234	Jauzac et al. (2020)
	MACS1931.8-2635	0.352	Caminha et al. (2019)
	MACS1115.9+0129	0.352	Caminha et al. (2019)
	MACS0429.6-0253	0.399	Caminha et al. (2019)
	MACS1206.2-0847	0.440	Richard et al. (2021)
	MACS0329.7-0211	0.450	Richard et al. (2021)
	RXJ 1347-1145	0.451	Richard et al. (2021)
	MACS1311.0-0310	0.494	Caminha et al. (2019)
	MACS1423.8+2404	0.545	Treu et al. (2015)
			Schmidt et al. (2014)
	MACS2129.4-0741	0.570	Jauzac et al. (2020)
RELICS	Abell 2163	0.2030	Rescigno et al. (2020)
	PLCK G171.9-40.7	0.2700	-
	Abell 2537	0.2966	Foëx et al. (2017)
	AbellS295	0.3000	Bayliss et al. (2016)
	MACSJ0035.4-2015	0.3520	-
	RXC J0949.8+1707	0.3826	-
	SMACSJ0723.3-7327	0.3900	-
	RXC J0032.1+1808	0.3956	-
	RXC J2211.7-0350	0.3970	-
	MACSJ0159.8-0849	0.4050	Stern et al. (2010)
	Abell 3192	0.4250	-
	MACSJ0553.4-3342	0.4300	Ebeling et al. (2017)
	MACSJ0417.5-1154	0.4430	Jauzac et al. (2019)
	RXC J0600.1-2007	0.4600	-
	MACSJ0257.1-2325	0.5049	Stern et al. (2010)
	ACT-CLJ0102-49151	0.8700	Sifón et al. (2013)

2.2.2 Photometric catalogs

We use the photometric catalogs of Kokorev and Brammer, et al. (in prep.; hereafter K&B catalogs), which include all 33 ALCS clusters. The K&B catalog uses HST+Spitzer/IRAC photometry and uses EAZY (Brammer et al., 2008) to derive photometric redshifts.

To use only the most reliable data from the photometric K&B catalogs we applied three filters:

1. A magnitude cutoff was added of 24 mag in the H-band. This was suggested by the authors of the catalogs. This cutoff is intended to remove contamination from blue faint galaxies and uncertain sources, since these sources will most likely be mistaken for low-redshift sources and therefore be assigned unphysical low values of SFR and stellar mass.

2. Sources with highly uncertain redshifts were removed, and only sources with $z_{\rm err}/z < 0.3$ were selected. The redshift error, z_{err}, was defined as the 1-σ error, i.e. the 16 percentile to 84 percentile error listed in the catalogs.

3. A sSFR cutoff was added of sSFR $> 3 \times 10^{-3}$ [Gyr^{-1}] for both cluster galaxies and field galaxies, to limit ourselves to star forming galaxies and to eliminate galaxies with large systematic errors.

For a better understanding of photometric redshift errors, we cross-matched our compiled spectroscopic and photometric catalogs using a 1 match radius. A comparison of the spectroscopic (zspec) and photometric (zphot) redshifts is shown in Fig. 2.2.1. For the sample used in this work (black dots) there is consistency in a broad sense, though we see significant photometric redshift errors ($\langle$(abs(zphot-zspec))/(1+zspec) $\rangle \approx 0.05$) for galaxies at z $\leq$1), plus highly erroneous redshifts in $\sim$10% of the galaxies.

We then combined the K&B photometric catalogs for the 33 clusters into a single photometric catalog, which we then divided into cluster and field galaxy sub-catalogs. Cluster galaxies were selected as those at $z \pm 0.1$ from the cluster redshift, and field galaxies as those which do not fulfil this condition. The $\pm$0.1 range is relatively small compared to the photometric redshift errors, but is used to avoid significant contamination of the galaxy cluster sub-sample. We thus obtained 1725 cluster galaxies between $0.0 < z < 1.0$ and 2468 field galaxies

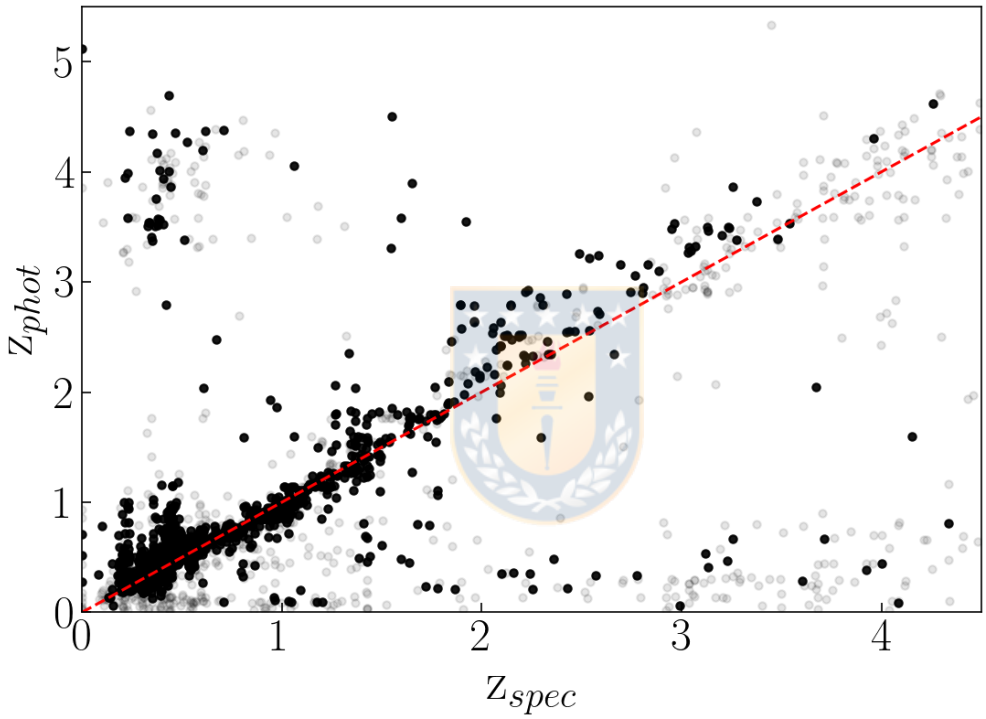

Figure 2.2.1: A comparison of photometric redshifts from the K&B catalogs versus spectroscopic redshifts from various catalogs (see references in Table 2.2.1). Black symbols show sources in the filtered photometric catalog we use, while grey symbols show the galaxies from the K&B catalog which were eliminated by us (see text). The red dashed line shows the line of equality for a better comparison.

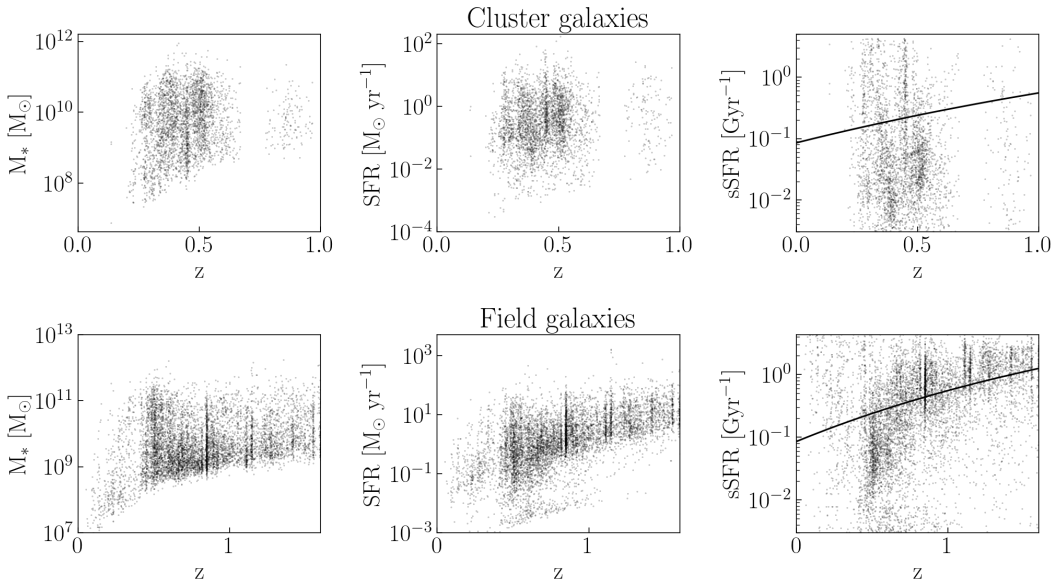

Figure 2.2.2: Stellar masses (left panels), SFR (middle panels) and sSFR (right panels), as a function of redshift, for all selected galaxies from the ALCS photometric catalog. The top row shows the cluster galaxies and the bottom row shows the field galaxies (see text). The black line in the right panels show the predicted redshift evolution of the main sequence (MS) of star formation from Elbaz et al. (2011).

between $0.0 < z < 1.6$, which fall inside the ALMA images of the clusters. Sources with higher redshift will be presented in Jolly et al. (in prep). Figure 2.2.2 shows the distribution of stellar mass, SFR and sSFR as a function of photometric redshift, for these cluster (top) and field (bottom) galaxies. The black line in the right panels shows the predicted redshift evolution of the main sequence (MS) of star formation from Elbaz et al. (2011).

Chapter 3

Methodology

3.1 Stacking softwares

We have developed continuum and spectral stacking software, which are made public here. Both can be used as a *task* within the Common Astronomy Software Applications package (CASA; McMullin et al. 2007), or as a standalone python script within CASA. Both primarily rely on python packages within CASA and are thus easy to install and update.

In either case, the softwares primarily relies on python packages within CASA and is thus easy to install and update. Further, the software is optimized to perform repeated stacks of very large datasets, where stacking requires to be re-run whenever a single or a few new images/cubes are added to the overall large set of input images/cubes. Intermediate results (e.g. extracted stamps or cubes of each source, observed and rest-frame spectra of each source) are saved to enable shorter runtimes when stacking is re-run with a few new images/cubes, to save memory when the stacking includes a large number of objects, to help review issues with the stacking results, and to help run Monte-Carlo simulations on the stacking results. For image stacking, algorithms are used to automatically identify individually detected sources and optionally leave them out of the stack. Finally, several useful plots and statistics are produced to help with the final analysis of the result.

3.1.1 Spectral Stacking Code

The spectral stacking code performs stacking within a list of data cubes provided by the user. The inputs are (a) a coordinate file with the positions (right ascension and declination in decimal degrees or radians), and redshifts of the targets to stack, and an optional column with weights for each source; (b) the datacubes to be used (specified by a fits file name and directory), which can be of different sizes and resolutions, and (c) the *stamp size*, i.e., the width in arcseconds of the square region to extract for stacking.

For each source in the coordinate file, the observed spectrum is extracted from the datacube (over an aperture of *stamp size*), and any continuum flux contribution is subtracted (by subtracting the median of the spectra). Intermediate results of this stage, e.g., the extracted spectra, sub-catalogs of sources for which the meaningful spectra were extracted, and those which do not fall within the ALMA datacubes, are stored as ascii files.

Extracted spectra are then converted to rest-frame (with an optional oversampling factor) and both a median- and mean-stacked spectrum is produced; intermediate results of this stage, e.g., all rest frame spectra, are stored in ascii files. After the stacking is performed, the code generates several plots to better understand and visualize the results. Plots created include individual spectra for each galaxy (observed and rest-frame), and the stacked spectrum over the entire frequency range or subplots for each 20 to 50 GHz window, and extracts of the stacked spectrum centered on known extragalactic emission lines.

Since intermediate ascii files are saved, when the stacking code is run again (e.g. when adding an extra cube to a previously stacked list of cubes), the user has the option to perform the extraction and conversion to rest-frame only for the new cube(s), and then combine the new and previous extractions to update the final stacked products. This is useful to stack a large number of cubes and reducing the time of extracting the observed spectra.

3.1.2 Continuum stacking

The continuum stacking task and script require a list of fits images to use (which can be of varying size and resolution), a coordinate file with the position (right ascension and declination in decimal degrees or radians) of each target, and

optionally a weight to be used for this target during stacking. The user also specifies the square *stamp size* in arcseconds to be used for sub-image extraction and stacking.

A continuum sub-image of *stamp size* is extracted for each source in the coordinate file, and these are saved into a fits cube where each channel of the cube corresponds to an individual source in the input coordinate catalog. This cube is later stacked using both the (weighted) mean and median method. Three stacks are created in each run: 'all-sources', 'only-detection' and 'only non-detection'. The first case includes all of the stamps. For the only-detection stack, an algorithm tests for all sources individually detected, according to a signal to noise ratio (SNR) determined by the user. If a detection is found in the central 1/3rd of the image, the stamp will be saved into a separate "only-detections" fits cube, and at the end of the process, a stacked image of the individual detections will be created. For the non-detection stack, the code selects the stamps in which sources are not individually detected, including centered and offset (i.e. detections on the edge of the stamp) detections. Then, optionally, stamps are rotated in multiples of 90 ° in order to cancel out striping or other correlated noise in the maps. Finally, the stamps are saved into a cube and stacked.

The resulting stacked images are saved to fits files and informative plots are produced. The plots show the average standard deviation $\bar{\sigma}$ for the stamps, the standard deviation σ of the stacked image and the number of stacked images (number of stamps). The stacked images are shown with and without smoothing. For each stacked image, a 2D Gaussian model is fitted to measure the peak flux and total flux density in the central 1/3rd of the stacked image.

3.2 SFRs, Dust masses and ISM masses from ALMA 1.2 mm fluxes

We derive SFRs from the observed-frame 1.2 mm ALMA images (individual images of detected sources or stacked images) as follows. First, we use the redshift (for individually detected sources) or median redshift of the stacked sample (for stacked detections) to derive a representative rest wavelength (1.2mm/(1+<z>) for the stacked image, and we test if this is closer to 350μm or 850μm. The measured flux in the stacked image is then extrapolated to the closest of the above two

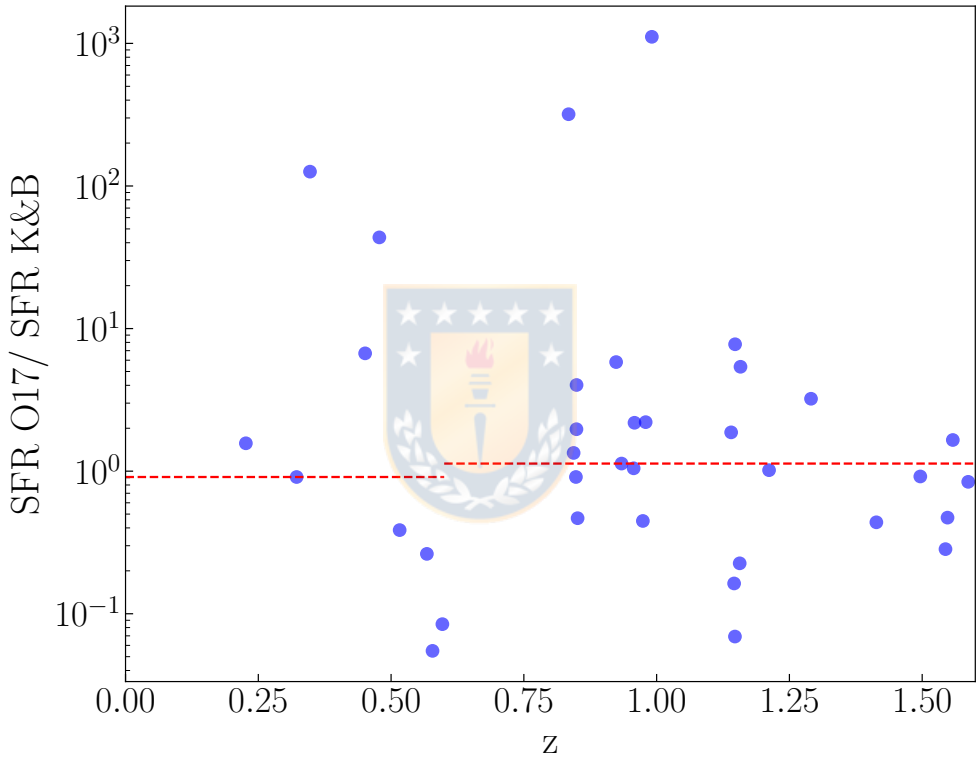

Figure 3.2.1: Ratio between SFRs derived from a single ALMA flux using our method (based on equations 3.2.1 to 3.2.4) and the SFRs listed in the K&B photometric catalogs, for individually detected sources from Fujimoto et al. (in prep). The sample was divided into two bins and we find the best median agreement (the red dashed lines) when using T = 21 K for sources at $0.0 < z < 0.6$ and T = 23 K for sources at $0.6 < z < 1.6$.

wavelengths assuming a greybody spectrum,

$$I_\nu = \mathrm{B}_\nu(T)\nu^\beta \tag{3.2.1}$$

where we fix $\beta = 1.8$; the value of T is calibrated further below in this sub-section.

The extrapolated flux at 350μm or 850μm is then converted into a specific luminosity L_ν [W Hz^{-1}] at either ν = 857 GHz or 353 GHz. This specific luminosity is in turn converted to an equivalent infrared luminosity $L_{\rm IR}$, using the equations of Orellana et al. (2017):

$$\begin{aligned} \log\left(\frac{L_{\rm IR}}{[L_\odot]}\right) &= 1.017\log\left(\frac{L_{350\mu m}}{[\mathrm{W\ Hz^{-1}}]}\right) \\ &+ 0.118\left(\frac{T_{\rm cold,\ dust}}{[K]}\right) - 16.45 \end{aligned} \tag{3.2.2}$$

$$\begin{aligned} \log\left(\frac{L_{\rm IR}}{[L_\odot]}\right) &= 1.01\log\left(\frac{L_{850\mu m}}{[\mathrm{W\ Hz^{-1}}]}\right) \\ &+ 0.15\left(\frac{T_{\rm cold,\ dust}}{[K]}\right) - 15.93 \end{aligned} \tag{3.2.3}$$

and where SFR is derived using the following equation, that uses the relationship of Kennicutt 1998 and assumes a Salpeter initial mass function,

$$SFR[M_\odot \mathrm{yr}^{-1}] = 1.78\times10^{-10} L_{\rm IR}[L_\odot] \tag{3.2.4}$$

The derived SFR for a source with constant flux (0.04 mJy in this example) using the above method, as a function of redshift, is shown in Fig. 3.2.2 (top panel). Here we used a constant dust temperature with redshift. Clearly, for z $\gtrsim$ 1, the estimated SFR (for the constant flux) is relatively independent of redshift: thus "SFR measurements" and "stacking" are effectively commutative at these redshifts. However, at z $\lesssim$ 1, the SFR of a constant flux source varies significantly with redshift, so the median SFR of several detected sources is not necessarily equivalent to the SFR obtained by first stacking the images, and then using the median flux and redshift to obtain the stacked SFR. Nevertheless, we argue that

this SFR derivation can also be used at z $\lesssim$ 1 for the following reasons.

The redshift distributions of each stellar mass sub-bin of each redshift bin are not significantly different in most bins. In the absence of strong systematic effects (evolution of temperature or SFR with redshift) we would expect that the process of stacking and then estimating the SFR via the mean redshift is not too different from first estimating individual SFRs and then later averaging. In fact, Fig. 3.2.2 shows that, for these redshift distributions, the mean SFR of the sample galaxies is similar to the stack-derived mean SFR, under the assumption that all sources have a roughly similar flux.

The remaining unknown is thus the temperature to be used in equations 3.2.1, 3.2.2 and 3.2.3. To calibrate this temperature (and its variation with redshift) we compared our derived SFRs to those listed in the K&B catalog. For this we selected 77 continuum sources individually detected in the ALCS fields at signal to noise ratios (SNR) > 5 (Fujimoto et al., in prep.), and used these fluxes to derive the 'obscured' SFR via our method (eqns. 1 to 4; hereafter the "O17" method). We divided the sample into two bins, $0 < z < 0.6$ and $0.6 < z < 1.6$, and found that our SFRs are in best agreement (in the median) with the K&B catalog SFRs when using a temperature $T = 21$ K for the lowest redshift bin, and $T = 23$ K for the second bin. Fig. 3.2.1 shows the ratio of our derived SFRs (from a single observed 1.2 mm flux) to the K&B catalog SFRs.

We use a linear interpolation between these calibrated temperatures in (the center of) each redshift bin to derive the SFR of any given stacked image (i.e. to derive the temperature at the median redshift of the sources which entered into the stack). Having calibrated dust temperatures by forcing median consistency between our ALMA-derived and previous SED-derived SFRs, we use these single component dust temperatures to estimate dust masses using the following equations from Orellana et al. (2017):

$$\log\left(\frac{M_{\rm dust}}{[M_\odot]}\right) = 0.940\log\left(\frac{L_{350\mu m}}{[\mathrm{W\ Hz^{-1}}]}\right) - 0.0791\left(\frac{T_{\rm cold,\ dust}}{[K]}\right) - 12.60 \quad (3.2.5)$$

$$\log\left(\frac{M_{\rm dust}}{[M_\odot]}\right) = 0.993\log\left(\frac{L_{850\mu m}}{[\mathrm{W\ Hz^{-1}}]}\right) - 0.054\left(\frac{T_{\rm cold,\ dust}}{[K]}\right) - 13.310 \quad (3.2.6)$$

This single-component dust temperature is also used, together with the observed 1.2 mm flux, to estimate the ISM mass (eqns 11 and 12 of Scoville et al., 2014), and the molecular gas mass (eqns A8, A11 and A14 of Scoville et al., 2016).

For individually detected or stacking detected CO emission lines, we convert the emission line flux into a molecular gas mass following Solomon et al. (1992), and using line ratios from Carilli and Walter (2013) to convert fluxes of higher CO rotational transitions into CO J:1-0 fluxes.

3.2.1 Commutativity of stacking vs. averaging

This subsection presents additional information on and tests on the conversion of (stacked) observed frame 1.2mm ALMA fluxes into dust masses, ISM masses, and SFRs.

We first test for consistency between mean estimates of individual SFRs, dust masses and ISM masses with the values derived from stacking, i.e. the value obtained from stacked fluxes and the mean redshift of the sub-sample. Figure 3.2.2 illustrates the conversion of a constant 1.2mm ALMA flux into SFR (top panel), dust mass (middle panel) and ISM mass (bottom panel) estimates at different redshifts. Here we use a source with flux 0.04mJy and black body temperature 22°, over the range of redshifts in our sample. At z>1 the estimations are relatively flat, but at z <1 the estimated quantity from the stack may not necessarily represent the median of the individual galaxies. We performed Monte-Carlo simulations using the redshift distributions within each of our redshift and stellar mass bins, assigning individual galaxies a flux uniformly distributed between 0 and and 120 μJy (the 2σ noise of the unstacked ALCS continuum maps). The resulting stacked

estimates in each MC iteration were compared to the median quantity of the individual galaxies, thus constraining the error of the former. These fractional errors are scaled to the flux value of 0.04mJy used in Fig. 3.2.2 and are plotted as error bars at the median redshift of each sub-sample (and colored by stellar mass bin) in Fig. 3.2.2. As can be seen in the figures both methods give relatively similar results. Thus we feel confident that within a redshift bin we can make meaningful comparisons between the results of each stellar mass bin.

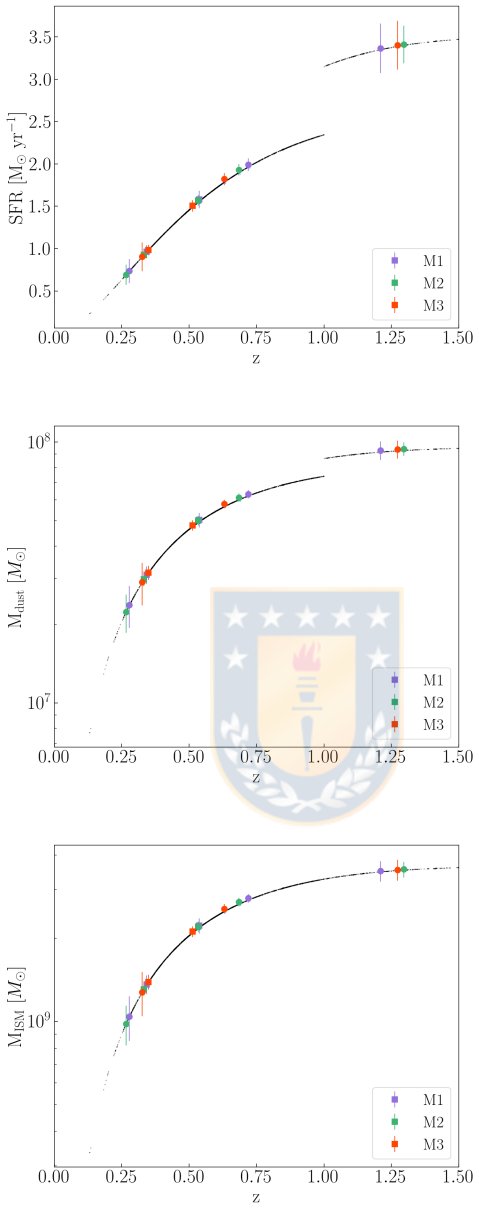

Figure 3.2.2: SFRs (top), dust masses (middle) and ISM mass (bottom) implied by a constant observed 1.2mm ALMA flux of 0.04 mJy over the redshift range of our sample galaxies (solid black line). A constant temperature of 22K is assumed at all redshifts. The jump at $z \sim 1$ is due to using equations 3.2.2 (3.2.3) at low (high) redshift. The symbols and error bars show the results of our MC simulations which compare the value derived from a stacked flux and median redshift, with the median value of the individual galaxies (see text). Symbols are plotted at the median redshift of each sub-sample and their colors follow the legend, with squares (circles) used for cluster (field) galaxies.

Chapter 4

Results

Our stacking codes provide mean and median stacked results (continuum and spectral stacking) for all sources, all individually detected sources, and all individually undetected sources. Even though the number of individual detections in the ALCS fields is relatively low, the crowded and clustered nature of our source catalog means that the few bright individually detected sources bias both the detected central flux, and the outskirts of the stacked maps. We thus, unless otherwise mentioned, use and present results based on mean stacking of extracted stamps which do not include stamps in which central or peripheral sources are individually detected. All stacks were performed without weighting.

4.1 Full sample stacks

To illustrate the power, and reliability, of stacking in the ALCS, we stacked all sources - cluster and field - in our moment 0 maps using the K&B catalogs with the extra filters described in Sect. 2.2.2, but for the full redshift range of the catalog, i.e., $0 < z < 12$. The left panel of Fig. **??** shows the continuum stacked maps of the individually non-detected sources (mean and median stacks).

The SNR is enhanced by $\sqrt{N}$, where N is number of objects stacked, as expected. The mean stacked continuum map of the individual non-detections has an rms of $\sigma_{stack} = 0.9\mu$Jy: equivalent to a $\sim$10 day integration with ALMA at 260 GHz.

Example spectral stacking results on the full sample are shown Fig. 4.1.2, which shows an illustrative excerpt of the spectral stack of all sources with high reliability

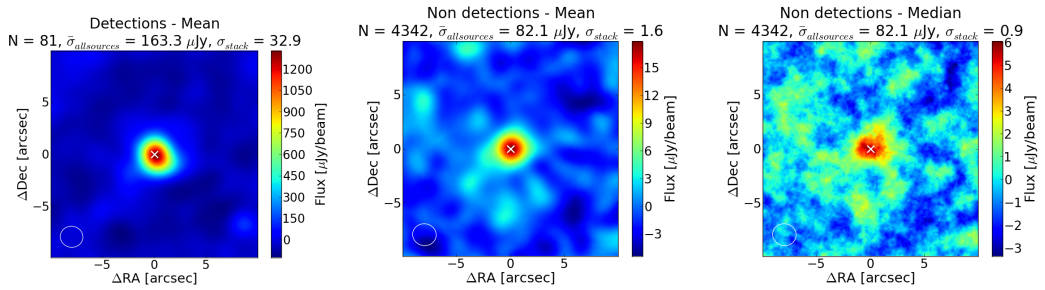

Figure 4.1.1: Images resulting from a continuum stack of all sources in our sample. The left panel shows the stack of all individually detected sources, the middle (right) panel shows the mean (median) stack of the individually non-detected sources. Above each panel, we show the number of sources stacked (N), the average rms of all input images which were stacked ($\bar{\sigma}_{all}$) and the rms of the final stacked image (σ_{stack}). The white crosses show the center of each image.

redshifts in which no line was individually detected. This demonstrates the large number of lines covered, and the clear decrease in the rms when large numbers of objects are stacked. While there is no clear line detection (further below we present a potential CO(4–3) stacked line detection in a high-SFR sub-sample), the figure demonstrates the power of stacking of ALMA datasets.

4.2 Spectral stacking in sub-samples

A stacked spectrum of all sources with individual detections of an emission line (Fujimoto et al., in prep) and for which high precision spectroscopic redshifts are available in the literature is shown in Fig. 4.2.1. This stacked profile shows broader wings as compared to a single Gaussian. While this could be a sign of outflows, it could be only an effect of redshift errors, so we do not further interpret the wings. The best fit Gaussian to the mean stacked spectrum gives a peak flux of 8.5 μJy and total flux of 2.9 Jy km/s, with a FWHM of 294 km/s.

The implied average molecular gas mass, using $L'_{CO\ J:3-2}/L'_{CO\ J:1-0} = 0.27$ (Carilli and Walter, 2013), is $M_{mol} = 3.1 \times 10^{10} M_{\odot}$ ($\alpha_{CO}/4.6$), where α_{CO} is in units of $M_{\odot}$ (K km/s pc^2)$^{-1}$, with a recommended value of 4.6 in normal star forming galaxies (Bolatto et al., 2013). Using the mean values of the SFRs and stellar masses of this sub-sample from the K&B catalog, the implied average SFE (SFE = SFR / M_{mol}) is SFE = 7.7×10^{-10}yr^{-1} ($4.6/\alpha_{CO}$) and the average molecular gas mass to average stellar mass ratio is 1.3 ($\alpha_{CO}/4.6$).

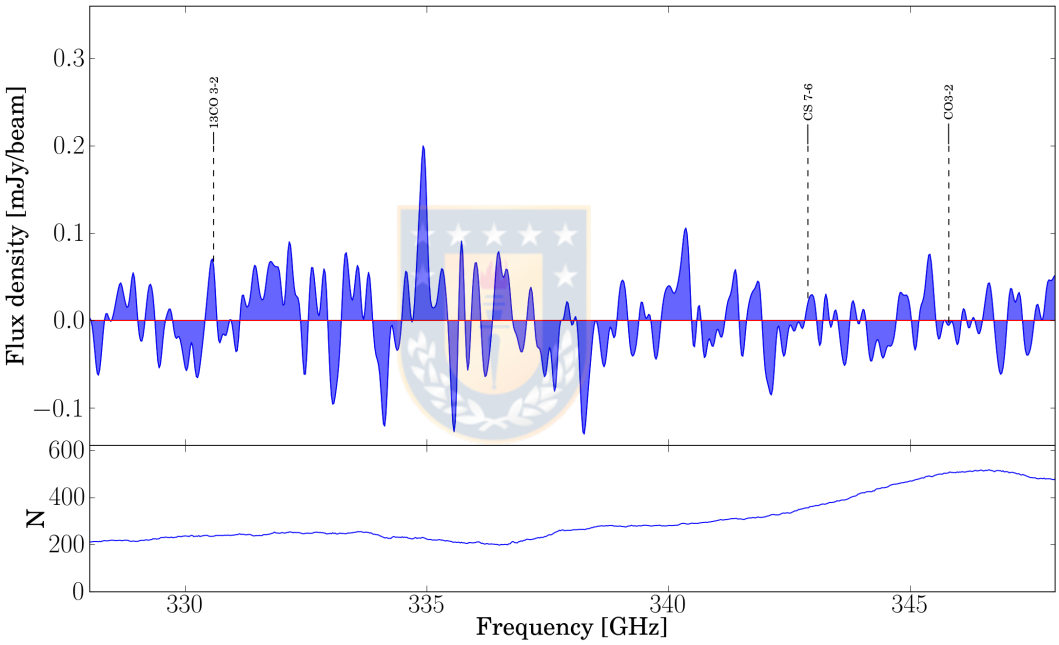

Figure 4.1.2: An excerpt of the frequency range from a spectral stack of all sources with high precision spectroscopic redshifts, which have no individually detected emission lines. The upper panel shows the stacked spectrum and the lower panel shows the number of objects stacked at each frequency.

Given that a spectral stack of all galaxies not individually detected in emission lines did not reveal stacked detections of any emission lines, we stacked a subsample of galaxies with the highest K&B catalog SFRs, and thus the highest expected molecular gas masses. To do this we cross matched our combined spectroscopic catalog with the combined K&B photometric catalog, and used the spectroscopic redshifts of the former and the SFR estimates of the latter. In this case, we did not use the cut-offs described in Sect. 2.2.2, since in this specific stacking analysis we do not use the photometric redshift, and are relatively robust to errors in the SFRs of the photometric ALCS catalog.

We then selected all sources in the uppermost 15-percentile of SFRs, with high accuracy spectroscopic redshifts and no individual line detections. The spectral stack of these sources is shown in the left panel of Fig. 4.2.2, with an emission line detected in at SNR 4.2 at the expected location of the CO J:4-3 line. The best fit Gaussian to the mean stacked spectrum gives a peak flux, total flux, and width of 0.3 mJy, 59 mJy km/s and 174 km/s respectively. Following the same procedure as the spectral stack of the individually detected emission line galaxies above, the implied mean molecular gas mass, using $L'_{CO\ J:4-3}/L'_{CO\ J:1-0} = 0.17$ (Carilli and Walter, 2013), is $M_{mol} = 3.1 \times 10^9 M_\odot\ (\alpha_{CO}/4.6)$. Using the mean SFRs and stellar masses of the stacked galaxies from the K&B catalogs, this implies an average star formation efficiency of $SFE = 1.4 \times 10^{-8} yr^{-1}\ (4.6/\alpha_{CO})$ and an average molecular gas to stellar mass ratio of $0.03\ (\alpha_{CO}/4.6)$.

Of the 10 galaxies which contributed to the stacked CO J:4-3 emission line, one galaxy has a potential individual detection of the CO J:4-3 line, which was not picked up in previous analyses. Eliminating this galaxy from the stack, weakens the CO J:4-3 detection to SNR ~ 3. This stacked is presented in Fig. 4.2.2, right panel. In this case the best fit Gaussian to the mean stacked spectrum gives a peak flux, total flux, and width of 0.27 mJy, 58 mJy km/s and 190 km/s respectively. If this is considered a 3σ upperlimit, the implied average molecular gas mass is $M_{mol} < 6 \times 10^9 M_\odot\ (\alpha_{CO}/4.6)$, average star formation efficiency $SFE < 7.9 \times 10^{-9} yr^{-1}\ (4.6/\alpha_{CO})$ and mean molecular gas to stellar mass ratio of $< 0.06\ (\alpha_{CO}/4.6)$.

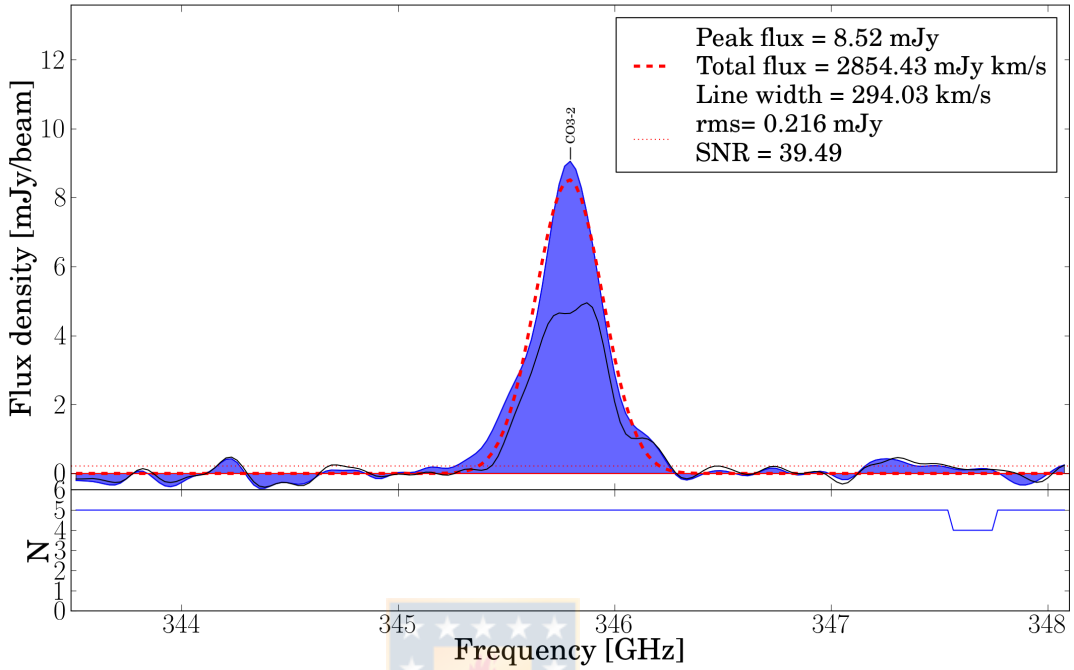

Figure 4.2.1: Spectral stacked CO J:3-2 spectrum of all sources in which this line is individually detected (Fujimoto et al., in prep.), and for which literature spectroscopic redshifts are available.

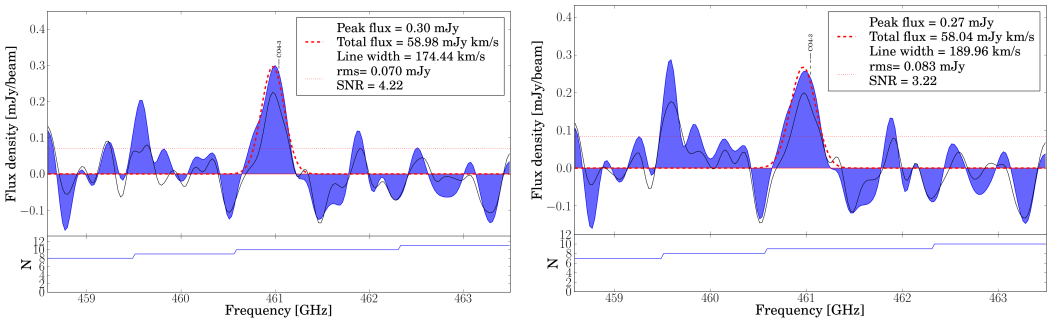

Figure 4.2.2: Spectral stack of individually undetected emission line sources in the uppermost (among all sources with an accurate spectroscopic redshift; see text) 15-percentile SFR bin. In both panels, the mean stacked profiles are shown in blue, the best fit Gaussian to this profile in red, and the median stack line profile in black. The bottom sub-panels show the number of objects stacked.

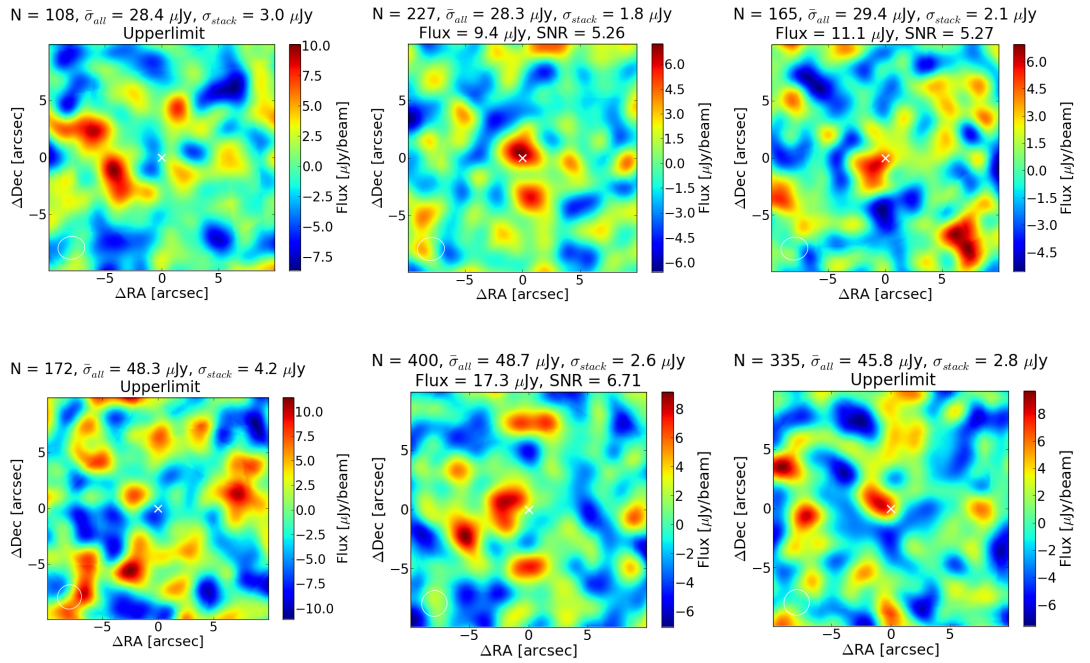

Figure 4.3.1: The mean-stacked continuum images of cluster galaxies, used to derive the fluxes shown in Fig. 4.3.3. The top row shows the stacked images for the redshift bin $0 < z_1 < 0.4$ and bottom row shows the stacked images for the redshift bin $0.4 < z_2 < 1.0$. Left panels correspond to the lowest stellar mass bin M_1, middle panels to the second stellar mass bin M_2, and right panels to the highest stellar mass bin M_3. At the top of each panel, we list the number of images which entered into the stack (N), the average rms of the input images ($\bar{\sigma}_{all}$), the rms of the stacked image (σ_{stack}) and the total flux of the fitted Gaussian.

4.3 Continuum-stacking: fluxes, dust and ISM masses

We divided both the cluster and field catalogs into bins of redshift and then sub-bins of stellar mass. The sizes, and ranges, of the bins were driven by the requirement of having sufficient sources in each bin in order to obtain meaningful stacked detections in a significant number of bins.

The cluster catalog was thus divided into two redshift bins, $0.0 < z_1 \leq 0.4$ (500 galaxies) and $0.4 < z_2 \leq 1.0$ (907 galaxies), and the field catalog was divided into three bins, $0.0 < z_1 \leq 0.4$ (63 galaxies), $0.4 < z_2 \leq 1.0$ (1489 galaxies) and $1.0 < z_3 \leq 1.6$ (354 galaxies). The highest redshift field bin was used primarily as a sanity check of our results at lower redshifts.

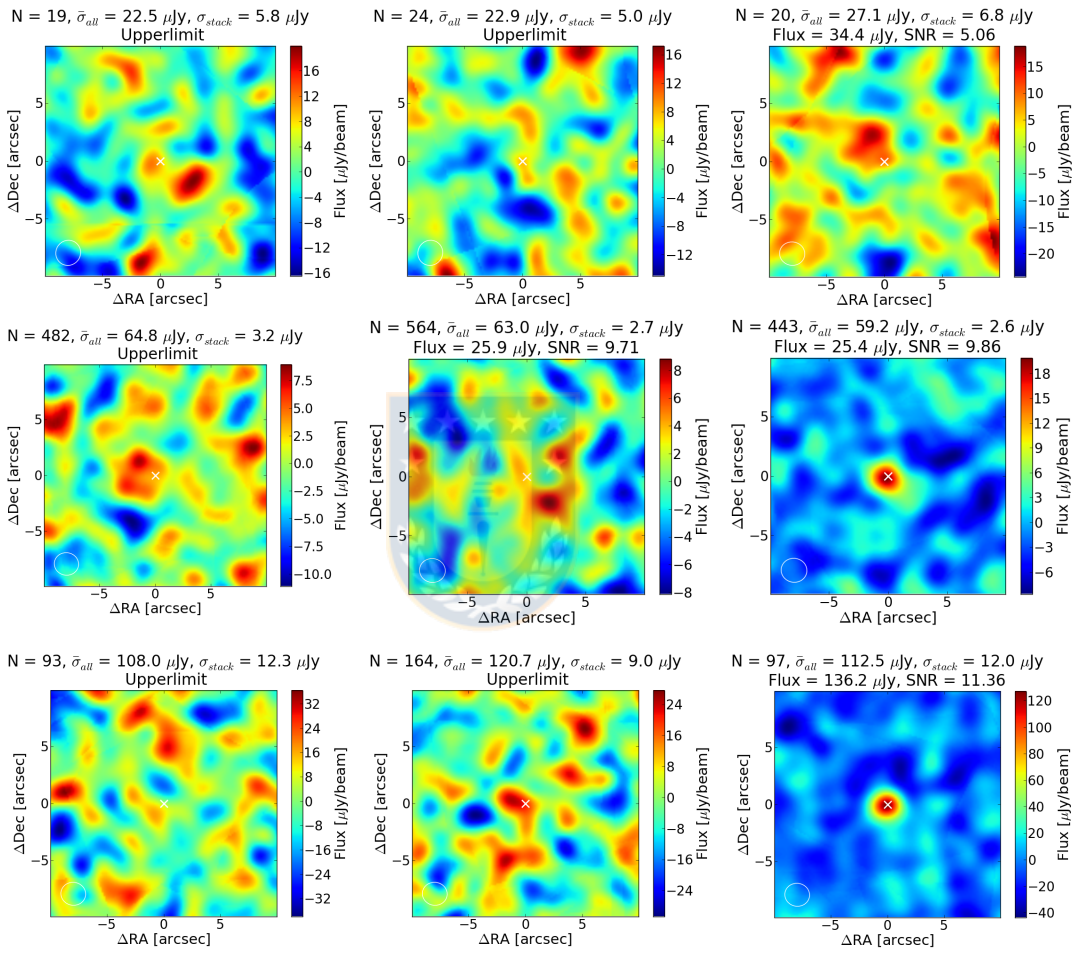

Figure 4.3.2: As in Fig. 4.3.1, but showing the stacked maps for field galaxies. The rows (top to bottom) correspond to the redshift bins $0 < z_1 < 0.4$, $0.4 < z_2 < 1.0$ and $1.0 < z_3 < 1.6$, respectively. The lowest stellar mass bin of the lowest redshift bin (top left panel) is considered a non-detection.

Each redshift bin was then sub-divided into three stellar mass bins: $10^9 < M_1 \leq 3 \times 10^9$, $3 \times 10^9 < M_2 \leq 2 \times 10^{10}$, $2 \times 10^{10} < M_3 \leq 4.6 \times 10^{11}$.

Figures 4.3.1 and 4.3.2 show the stacked maps obtained for all cluster, and field, galaxy stacks, in the redshift and stellar mass bins above, respectively. Two dimension Gaussian fits to these stacked maps were used to test for detections and then extract the peak and total flux of the central source in the case of a detection. We considered a stacked map to have a detection if (a) the Gaussian fit revealed a $\geq 5\sigma$ detection in total flux; (b) the fitted Gaussian peak was within 25 of the central pixel of the stacked map; and (c) the smoothed (with a 1 box kernel) stacked map showed no other $\geq 5\sigma$ detections in the central 8, and there was no more than one other source stronger than the central detection in the 20×20 stacked FOV. In the case of a non-detection, we use a flux upperlimit of 5σ, where σ was calculated over the 20×20 stacked FOV; in one case (left column, middle row of Fig. 4.3.2) we use a 6σ upperlimit as we potentially detected a 5σ source close to the center (this detection was rejected due to criterion (c) above).

The 1.2 mm flux (the total flux of the Gaussian fit) or upperlimit for each redshift bin in these stacked maps, as a function of stellar mass bin, are shown in Fig. 4.3.3.

Dust masses derived from the ALMA 1.2mm fluxes are shown in Fig. 4.3.4. Since the conversion between the y-axes of these two panels is almost linear, the results are similar. For the two redshift bins at $z \leq 1.0$, dust masses are flat or decrease with increasing stellar mass, for both cluster and field galaxies. It is only in the highest (field-only) redshift bin that dust masses increase with stellar mass. Our results are consistent with higher dust masses in field galaxies as compared to cluster galaxies, in most bins, though the differences may be as low as a factor of few. For the highest stellar mass bin in field galaxies, the dust mass increases monotonically with redshift, but the equivalent behavior of cluster galaxies is not clear.

The left panel of Figure 4.3.5 shows the redshift evolution of f_{dust} (the dust to stellar mass ratio) and compares them with the expected values from Liu et al. (2019), assuming a dust to gas ratio of 0.01. The mean f_{dust} of the field galaxies in our sample (empty symbols) fall relatively near the expectations of galaxies living on the dividing line between star-forming MS galaxies and passive galaxies,

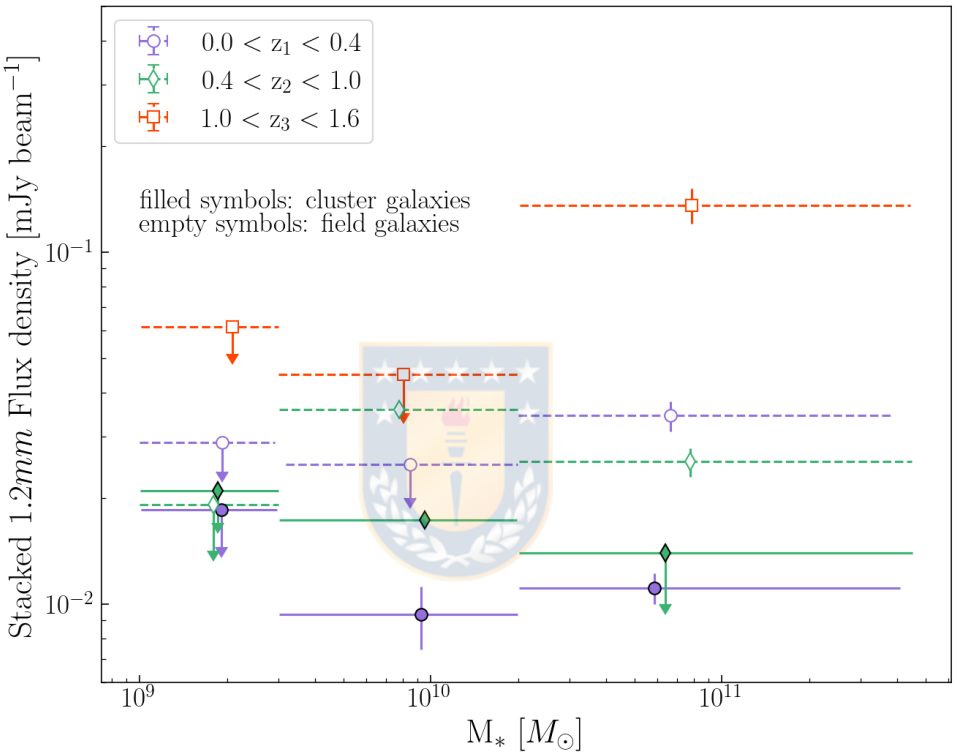

Figure 4.3.3: The 1.2mm flux in the mean-stacked continuum map of all individually non-detected sources, as a function of the K&B catalogue stellar mass, for each redshift bin. Cluster (field) galaxy stacks are shown with filled (open) symbols. Symbols and colors distinguish each redshift bin: purple circles for $0 < z_1 \leq 0.4$, green diamonds for $0.4 < z_2 \leq 1.0$ and red squares for $1.0 < z_3 \leq 1.6$. One sigma errors in flux are shown (these are smaller than the symbol size when not visible), and downward pointing arrows typically denote (5σ) upperlimits (see text). The horizontal 'error bars' of each symbol denote the stellar mass range of galaxies in that bin.

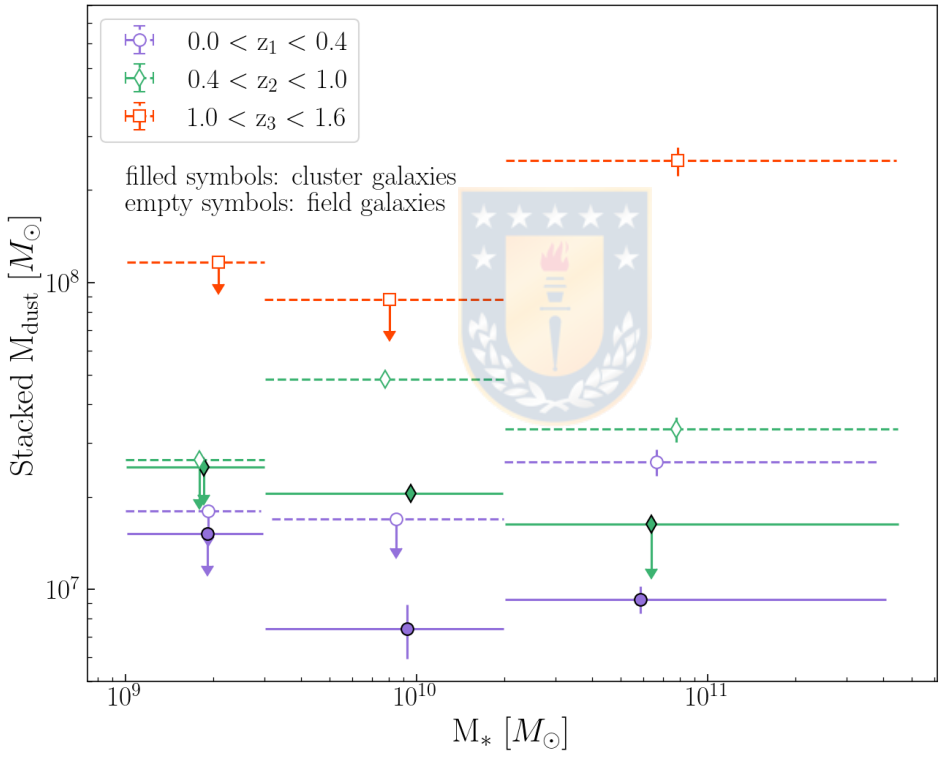

Figure 4.3.4: As in Fig. 4.3.3 but for the 1.2 mm stack-derived dust masses.

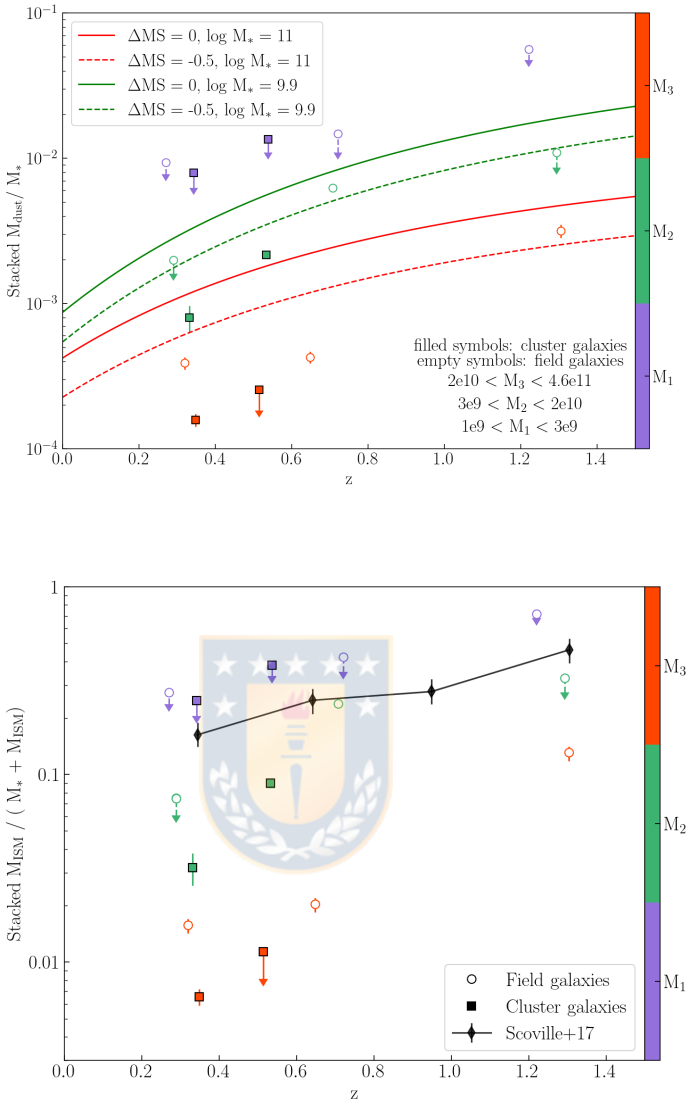

Figure 4.3.5: Left: The stacked dust to stellar mass ratio (left panel; M_{dust} from the stacked 1.2 mm flux and the mean M_* from the K&B catalogs) as a function of redshift for all redshift and stellar mass bins and for both cluster (squares) and field (circles) galaxies. Colors distinguish stellar mass bins: purple, green, and red symbols are used for the lowest, middle, and highest stellar mass bins. Downward pointing triangles denote upper limits. The overlaid lines show the expected values (Liu et al., 2019, using a dust to gas ratio of 0.01) for galaxies in the MS (solid; SFR = SFR_{MS}) and 0.5 dex below the MS (dashed; SFR $\sim 0.3 \times$ SFR_{MS}) for a galaxy with log M_* = 11.0 (red) and 9.9 (green), which correspond to the bin midpoints of our middle and high stellar mass bins. Right: As in the left panel, but for the ISM mass fraction (ISM mass to stellar plus ISM mass ratio) as a function of redshift. Black diamonds and their error bars show the gas mass fractions derived by Scoville et al. (2017) for star-forming log $M_\star \sim 11$ galaxies in the COSMOS field; these points are connected for easier visualization.

implying a roughly equal number of star forming and passive galaxies in each bin. However, the mean f_{dust} of the cluster galaxies in our sample (filled symbols) fall significantly lower than the expectation of the dividing line between MS and passive galaxies. That is, these cluster sub-samples are likely dominated by passive, rather than star forming, galaxies.

The right panel of Figure 4.3.5 shows the gas fraction ($f_{\rm ISM} = {\rm M_{ISM}}/({\rm M_*} + {\rm M_{ISM}})$) as a function of redshift for our sample bins, and compares these with the fractions seen in log ${\rm M_*} \sim 11$ galaxies from the COSMOS field (Scoville et al., 2017). Note that ${\rm M_{ISM}}$ is derived from our stacked 1.2 mm fluxes and K&B catalog ${\rm M_*}$s. Our highest stellar mass bins (2E10<$\rm M_3$ ≤4.6E11) at all redshifts, and for both cluster and field galaxies (red symbols), are one dex lower than the mean values of Scoville et al. (2017) (except for the highest redshift field bin which is only ∼3 lower) even though they have similar stellar masses. The discrepancy lessens for the intermediate (3E9<$\rm M_2$ ≤2E10) stellar mass bin, and the upper limits in the lowest stellar mass bin (1E9<$\rm M_1$ ≤3E9) align well with the COSMOS values, and so could potentially be consistent with the COSMOS values.

4.3.1 Continuum-stacking: SFR, sSFR, and SFE

The 1.2 mm stacked fluxes shown in Fig. 4.3.3 were converted into SFRs using the mean redshift of each sub-sample and our SFR conversion method. The results are shown in the left (cluster galaxies) and right (field galaxies) panels of Fig. 4.3.6. Besides plotting our 1.2 mm-stacked SFRs (filled symbols), we also show the mean SFRs of all galaxies in each bin from the K&B photometric catalogs (equivalent unfilled symbols) and the expected MS from Speagle et al. (2014) for each redshift bin.

In the highest stellar mass bin (2E10<$\rm M_3$ ≤4.6E11) the K&B catalog (unobscured) SFRs are 1 dex higher than the 1.2 mm-stacked (obscured) SFRs, for both cluster and field galaxies. The K&B catalog (unobscured) SFRs increase with increasing stellar mass in all redshift bins, and for both cluster and field galaxies, though the increase is not as large as that expected from the Speagle et al. (2014) MS for most bins. However, our 1.2 mm-stacked SFRs show a flat or downturn with increasing stellar mass except for the highest redshift and highest stellar mass field bin. Comparing the cluster and field MSs, we see that the K&B (unobscured) SFRs of field galaxies are slightly higher than those of cluster galaxies for most

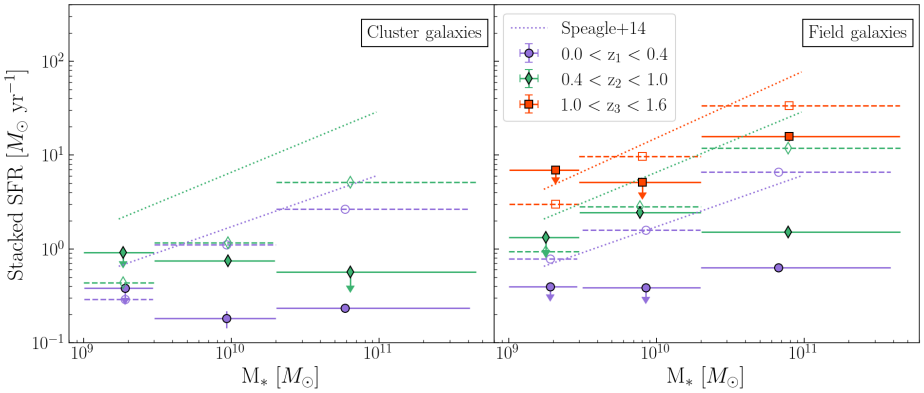

Figure 4.3.6: As in Fig. 4.3.3 but showing the dependence of SFR as a function of stellar mass. The filled symbols are the same as Fig. 4.3.3. The equivalent (symbol and color) empty symbols with their dashed horizontal lines, show the mean SFRs of the galaxies in the bin from the K&B photometric catalogs. The dotted colored lines, in the corresponding colors, show the expected MS of Speagle et al. 2014 for each redshift bin.

bins. However, we cannot distinguish a clear difference between cluster and field galaxies when considering the 1.2 mm stacked SFRs.

To better visualize the evolution of sSFR with redshift Fig. 4.3.7 re-plots the data of Fig. 4.3.6, and compare our datapoints to the expected evolution of the MS with redshift (Elbaz et al., 2011; Speagle et al., 2014). Overall, the sSFRs of both cluster and field samples are $\sim$ 1 dex lower than expectations at the lowest redshifts, but the difference decreases at intermediate and higher redshifts. Also, the disagreement becomes less extreme with decreasing stellar mass.

The right panel of Fig. 4.3.7 shows the star formation efficiency (SFE = SFR / M_{mol}; right panel) as a function of redshift for our galaxies, and compares these with the results of Tacconi et al. (2018). Here the SFE was derived using the SFR from the K&B photometric catalogs and the molecular mass derived from the stacked 1.2 mm fluxes. Within factor of a few, our galaxies are consistent with the predictions of Tacconi et al. (2018), though the highest stellar mass bin shows a factor $\sim$5 larger SFEs for both low redshift cluster and field galaxies.

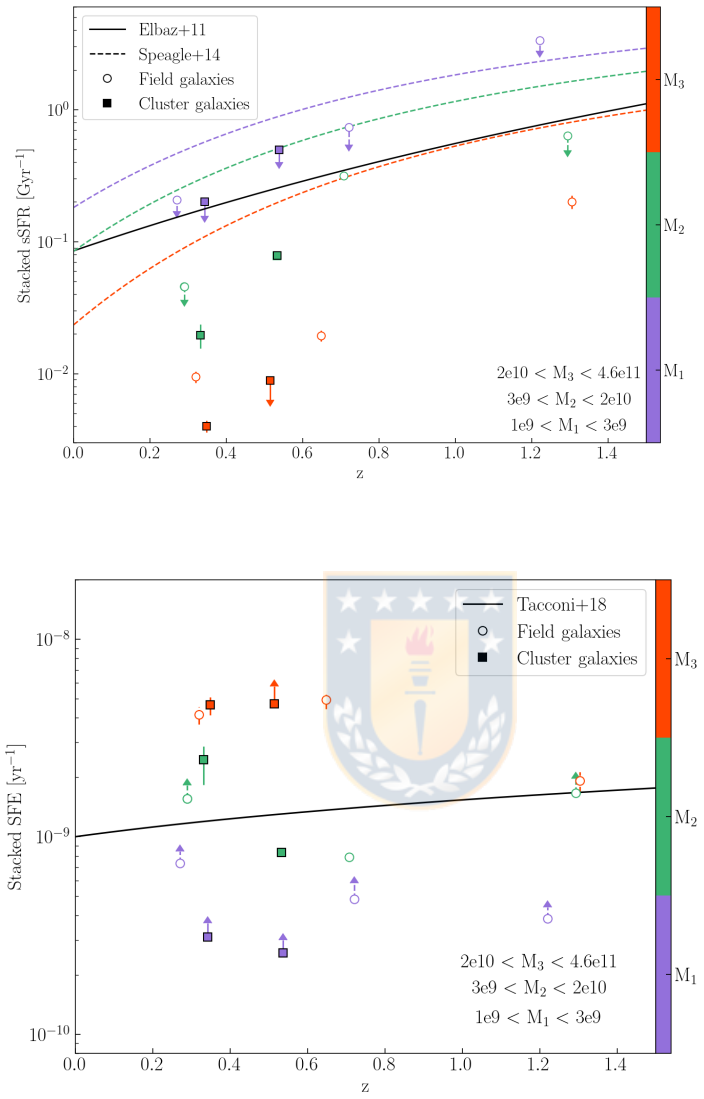

Figure 4.3.7: Specific SFR (sSFR; left panel) and star formation efficiency (SFE; right panel) as a function of redshift, for cluster (squares) and field (circles) stacks. Colors distinguish stellar mass bins: purple, green, and red symbols are used for the lowest, middle, and highest stellar mass bins. Downward pointing triangles denote upper limits. In the left panel, the sSFR is derived from the 1.2 mm stacked flux and the K&B stellar mass. The solid black line shows the Elbaz et al. (2011) main sequence evolution with redshift, and the colored curves show the MS for each stellar mass bin following Speagle et al. (2014). In the right panel, the SFE is derived from the K&B SFR and the 1.2 mm stacked flux derived gas mass, and the solid line shows the relationship of SFE with redshift derived by Tacconi et al. (2018) in the PHIBBS sample (SFE $\propto t_{\rm depl}{}^{-1}$).

Chapter 5

Discussion and Conclusions

5.1 Discussion

The ALCS data have significant legacy value, and comprehensive spectroscopic redshifts in all 33 cluster fields will greatly enhance the science exploitation of these ALMA data. Even with current spectroscopic and photometric catalogs our stacking analysis already enables a glimpse into the average properties of cluster and field galaxies, with indications that the average stacked properties are significantly different from the average properties of individual detections. Since our 1.2 mm continuum stacking uses bins of redshift and stellar mass, each bin stacks both star-forming and passive galaxies together, so that a low stacked SFR could imply an across-the-board low SFR in individual galaxies, or a large fraction of passive galaxies in the bin.

Spectroscopic stacking of the CO J:4-3 line in ten high-SFR (where the SFR was taken from the K&B catalogs, thus tracing relatively unobscured star formation) galaxies reveal relatively low gas reservoirs with a molecular gas to stellar mass ratio of $\sim$3% (or $\lesssim$6%). In contrast, stacking the individually detected CO lines give very high values of M_{mol}/M_* ($\sim$100%), though this high value could be due the photometric catalogues underestimating the stellar masses of cluster cD galaxies.

The continuum stacking in redshift and stellar mass bins reveal several interesting results. In general the average obscured SFRs (from the 1.2mm stacking) are lower than the average unobscured SFRs (from the K&B catalog - derived from spectral

fitting of optical to near-IR data). While the K&B (unobscured) SFRs more closely follow the expected MS of star formation, the 1.2 mm stacks (obscured star formation) do not. Cluster stacks consistently show factor few lower fluxes (thus lower estimated dust masses, ISM masses, and obscured SFRs) as compared to field galaxies: indicating weaker SFRs across the board, or a larger fraction of passive galaxies in clusters.

Comparing our stacked results to existing literature values, which are based primarily on individually detected galaxies, we consistently see that the highest stellar mass bin, for both cluster and field galaxies, shows lower dust and ISM masses, and lower SFRs. The same appears true, though at a smaller level, for galaxies in the intermediate mass bin.

We use a relatively low (single component) dust temperature (21–23 K) for our conversions of stacked flux to dust and ISM mass, and SFRs. These temperatures lie between those of passive and star forming galaxies at these redshifts, but closer to the former. Increasing our assumed dust temperatures will result in lower dust and ISM masses, and SFRs. Thus the lower masses and/or turnovers found here are relatively robust to the assumed dust temperature.

5.2 Conclusions

We have performed a stacking analysis within the ALMA Cluster Survey fields, using new continuum and spectral stacking software, which is made public here.

We performed continuum stacking of the 1.2mm flux for 1407 cluster and 1906 undetected field galaxies at intermediate redshifts ($0.2 < z < 0.9$), in multiple redshift bins over z = 0.2–1.6, each with three stellar mass bins over log M_* [$M_\odot$] = 9-11.7. We also performed spectral stacking of individually detected emission lines and a high SFR-selected sub-samples of individually non-detected galaxies.

For the spectral stacking we find a potential stacked line detection of the CO J:4-3 emission line (SNR ~ 4), among high SFR galaxies. For this line we derived the average molecular gas mass of $M_{\rm mol} = 3.1 \times 10^9 M_\odot$, average SFE = 1.4×10^{-8} yr^{-1} and average gas-to-stellar ratio of 0.003. Since we identified a galaxy with a potential detection of the CO J:4-3 line among the stacked galaxies (which was not identified before), we also performed a stack without this galaxy. Given

the lower SNR in the detection in this case we considered this stack as a 3σ upperlimit, yielding an average molecular gas mass of $M_{\rm mol} < 6 \times 10^9 M_\odot$, average SFE $< 7.9 \times 10^{-9}$ yr^{-1} and average gas-to-stellar ratio of < 0.006.

Our continuum stacked 1.2 mm fluxes are used to estimate average dust masses, ISM masses and SFRs, allowing us to contrast the average properties of cluster and field galaxies, and their evolution with stellar mass and redshift.

The conversion of stacked 1.2 mm fluxes to masses and SFRs assumes a (single component) dust temperature and grey body spectral index, and is done at the mean redshift (thus luminosity distance and observed frequency) of the stacked sub-sample. We calibrated the dust temperature, and its evolution with redshift, using detected 1.2 mm continuum sources, and used Monte Carlo simulations to show that the process of deriving our mean properties are relatively commutative in the samples used here, i.e. the mean value of a simulated sample agrees with the value derived from the stacked flux; these differences are smaller than the observed differences between bins.

When comparing cluster versus field galaxies, we see the following. Field galaxies show higher dust masses, that increase with redshift in the highest stellar mass bin (2E10 $<$M$_3$ $\leq$ 4.6E11). Their dust to stellar mass fractions are closer to the expected fractions for MS star-forming galaxies than cluster galaxies, likely implying that our cluster sub-samples are dominated by passive galaxies. They also show slightly higher unobscured SFRs than cluster galaxies and fall closer to the expected MS.

Both cluster and field galaxies show lower continuum-estimated gas fractions when compared to log M$_*$ $\sim$ 11 galaxies from Scoville et al. (2017), lower sSFRs when compared to the MSs of Elbaz et al. (2011); Speagle et al. (2014) and mostly similar SFEs to those in Tacconi et al. (2018) (except for the highest stellar mass bin of low redshift galaxies, which shows larger values).

In terms of redshift evolution, we find that the difference between the stacked galaxies sSFRs and the expected MS for star forming galaxies decreases with higher redshifts and lower stellar mass. A similar behaviour is seen for the dust and gas fractions, where the disagreement with the MS decreases with higher redshifts.

While our results require to be confirmed with more comprehensive and accurate

catalogs of redshift and stellar mass for the ALCS clusters, are already find lower average ISM mass fractions, dust mass fractions, SFR and sSFRs than those than average values found for individually detected galaxies.

Bibliography

Annunziatella, M., Mercurio, A., Biviano, A., et al. (2016). *A&A*, 585: A160.

Bayliss, M. B., Ruel, J., Stubbs, C. W., Allen, S. W., Applegate, D. E., Ashby, M. L. N., Bautz, M., et al. (2016). , 227:3.

Bianconi, M., Smith, G. P., Haines, C. P., McGee, S. L., Finoguenov, A., and Egami, E. (2020). LoCuSS: exploring the connection between local environment, star formation, and dust mass in Abell 1758. , 492(4):4599–4612.

Bolatto, A. D., Wolfire, M., and Leroy, A. K. (2013). The CO-to-H_2 Conversion Factor. , 51(1):207–268.

Boselli, A. and Gavazzi, G. (2006). Environmental Effects on Late-Type Galaxies in Nearby Clusters. , 118(842):517–559.

Boselli, A. and Gavazzi, G. (2014). On the origin of the faint-end of the red sequence in high-density environments. , 22:74.

Brammer, G. B., van Dokkum, P. G., and Coppi, P. (2008). EAZY: A Fast, Public Photometric Redshift Code. , 686(2):1503–1513.

Cairns, J., Stroe, A., De Breuck, C., Mroczkowski, T., and Clements, D. (2019). Large Molecular Gas Reservoirs in Star-forming Cluster Galaxies. , 882(2):132.

Caminha, G. B., Rosati, P., Grillo, C., et al. (2019). Strong lensing models of eight CLASH clusters from extensive spectroscopy: Accurate total mass reconstructions in the cores. , 632:A36.

Carilli, C. L. and Walter, F. (2013). *ARA&A*, 51: 105.

Chen, C.-C., Hodge, J. A., Smail, I., Swinbank, A. M., Walter, F., Simpson, J. M., Calistro Rivera, G., Bertoldi, F., Brandt, W. N., Chapman, S. C., da Cunha, E., Dannerbauer, H., De Breuck, C., Harrison, C. M., Ivison, R. J., Karim, A., Knudsen, K. K., Wardlow, J. L., Weiß, A., and van der Werf, P. P. (2017). A Spatially Resolved Study of Cold Dust, Molecular Gas, H II Regions, and Stars in the z = 2.12 Submillimeter Galaxy ALESS67.1. , 846(2):108.

Cimatti, A., Cassata, P., Pozzetti, L., Kurk, J., et al. (2008). *A&A*, 482: 21.

Coe, D., Salmon, B., Bradač, M., Bradley, L. D., et al. (2019). *ApJ*, 884:85C.

Delhaize, J., Meyer, M. J., Staveley-Smith, L., and Boyle, B. J. (2013). *MNRAS*, 433: 1398.

Domínguez Sánchez, H., Bernardi, M., et al. (2019). *MNRAS*, 489: 5612.

Ebeling, H., Qi, J., and Richard, J. (2017). , 471:3305–3322.

Elbaz, D., Daddi, E., Le Borgne, D., Dickinson, M., Alexander, D. M., Chary, R. R., Starck, J. L., Brandt, W. N., Kitzbichler, M., MacDonald, E., Nonino, M., Popesso, P., Stern, D., and Vanzella, E. (2007). The reversal of the star formation-density relation in the distant universe. , 468(1):33–48.

Elbaz, D., Dickinson, M., Hwang, H. S., Díaz-Santos, T., Magdis, G., Magnelli, B., Le Borgne, D., Galliano, F., et al. (2011). , 533:A119.

Elson, E. C., Baker, A. J., and Blyth, S. L. (2019). On the uncertainties of results derived from H I spectral line stacking experiments. , 486(4):4894–4903.

Fabello, S., Catinella, B., Giovanelli, R., et al. (2011). *MNRAS*, 411: 993.

Foëx, G., Chon, G., and Böhringer, H. (2017). , 601:A145.

Fornasini, F. M., Kriek, M., Sanders, R. L., et al. (2019). *ApJ*, 885: 65.

Franco, M., Elbaz, D., Béthermin, M., Magnelli, B., Schreiber, C., Ciesla, L., Dickinson, M., Nagar, N., Silverman, J., et al. (2018). , 620: A152.

Geller, M. J., Hwang, H. S., Diaferio, A., Kurtz, M. J., Coe, D., and Rines, K. J. (2014). , 783: 52.

González-López, J., Bauer, F. E., Romero-Cañizales, C., Kneissl, R., Villard, E., Carvajal, R., Kim, S., Laporte, N., Anguita, T., Aravena, M., Bouwens, R. J., Bradley, L., Carrasco, M., Demarco, R., Ford, H., Ibar, E., Infante, L., Messias, H., Muñoz Arancibia, A. M., Nagar, N., Padilla, N., Treister, E., Troncoso, P., and Zitrin, A. (2017). The ALMA Frontier Fields Survey. I. 1.1 mm continuum detections in Abell 2744, MACS J0416.1-2403 and MACS J1149.5+2223. , 597:A41.

Grillo, C., Karman, W., Suyu, S. H., Rosati, P., et al. (2016). *ApJ*, 822: 78.

Hodge, J. A., Karim, A., Smail, I., Swinbank, A. M., Walter, F., Biggs, A. D., Ivison, R. J., Weiss, A., Alexander, D. M., Bertoldi, F., Brandt, W. N., Chapman, S. C., Coppin, K. E. K., Cox, P., Danielson, A. L. R., Dannerbauer, H., De Breuck, C., Decarli, R., Edge, A. C., Greve, T. R., Knudsen, K. K., Menten, K. M., Rix, H. W., Schinnerer, E., Simpson, J. M., Wardlow, J. L., and van der Werf, P. (2013). An ALMA Survey of Submillimeter Galaxies in the Extended Chandra Deep Field South: Source Catalog and Multiplicity. , 768(1):91.

Jauzac, M., Klein, B., Kneib, J.-P., Richard, J., Rexroth, M., Schäfer, C., and Verdier, A. (2020). *arXiv e-prints*, page arXiv:2006.10700.

Jauzac, M., Mahler, G., Edge, A. C., Sharon, K., Gillman, S., Ebeling, H., Harvey, D., et al. (2019). , 483:3082–3097.

Jolly, J.-B., Knudsen, K. K., and Stanley, F. (2020). LINESTACKER: a spectral line stacking tool for interferometric data. , 499(3):3992–4010.

Karman, W., Caputi, K. I., Caminha, G. B., Gronke, M., Grillo, C., Balestra, I., Rosati, P., Vanzella, E., Coe, D., et al. (2017). , 599:A28.

Kennicutt, Robert C., J. (1998). *ApJ*, 498: 541.

Liu, D., Schinnerer, E., Groves, B., Magnelli, B., Lang, P., Leslie, S., Jiménez-Andrade, E., Riechers, D. A., Popping, G., Magdis, G. E., Daddi, E., Sargent, M., Gao, Y., Fudamoto, Y., Oesch, P. A., and Bertoldi, F. (2019). Automated Mining of the ALMA Archive in the COSMOS Field (A^{3}COSMOS). II. Cold Molecular Gas Evolution out to Redshift 6. , 887(2):235.

Lotz, J. M., Koekemoer, A., Coe, D., et al. (2017). *ApJ*, 837: 97L.

Maddox, N., Hess, K. M., Blyth, S. L., and Jarvis, M. J. (2013). Comparison of H I and optical redshifts of galaxies - the impact of redshift uncertainties on spectral line stacking. , 433(3):2613–2625.

Magnelli, B., Boogaard, L., Decarli, R., Gónzalez-López, J., Novak, M., Popping, G., Smail, I., Walter, F., Aravena, M., Assef, R. J., Bauer, F. E., Bertoldi, F., Carilli, C., Cortes, P. C., Cunha, E. d., Daddi, E., Díaz-Santos, T., Inami, H., Ivison, R. J., Fèvre, O. L., Oesch, P., Riechers, D., Rix, H.-W., Sargent, M. T., Werf, P. v. d., Wagg, J., and Weiss, A. (2020). The ALMA Spectroscopic Survey in the HUDF: The Cosmic Dust and Gas Mass Densities in Galaxies up to z $\sim$ 3. , 892(1):66.

Maltby, D. T., Almaini, O., McLure, R. J., et al. (2019). *MNRAS*, 489: 1139.

McCracken, H. J., Milvang-Jensen, B., et al. (2012). *A&A*, 544: A156.

McMullin, J. P., Waters, B., Schiebel, D., Young, W., and Golap, K. (2007). volume 376 of *Astronomical Society of the Pacific Conference Series*, page 127M.

Morokuma-Matsui, K., Kodama, T., Morokuma, T., Nakanishi, K., Koyama, Y., Yamashita, T., Koyama, S., and Okamoto, T. (2021). A Phase-space View of Cold-gas Properties of Virgo Cluster Galaxies: Multiple Quenching Processes at Work? , 914(2):145.

Netzer, H., Lani, C., Nordon, R., et al. (2016). *ApJ*, 819: 123.

Orellana, G., Nagar, N. M., Elbaz, D., Calderón-Castillo, P., Leiton, R., Ibar, E., Magnelli, B., Daddi, E., Messias, H., Cerulo, P., and Slater, R. (2017). *A&A*, 602: A68.

Oteo, I., Zwaan, M. A., Ivison, R. J., Smail, I., and Biggs, A. D. (2016). ALMACAL I: First Dual-band Number Counts from a Deep and Wide ALMA Submillimeter Survey, Free from Cosmic Variance. , 822(1):36.

Paccagnella, A., Vulcani, B., Poggianti, B. M., Moretti, A., Fritz, J., Gullieuszik, M., Couch, W., Bettoni, D., Cava, A., D'Onofrio, M., and Fasano, G. (2016). Slow Quenching of Star Formation in OMEGAWINGS Clusters: Galaxies in Transition in the Local Universe. , 816(2):L25.

Perger, K., Frey, S., Gabányi, K. É., et al. (2019). *MNRAS*, 490: 2542.

Pimbblet, K. A. (2003). *PASA*, 20: 294.

Popesso, P., Rodighiero, G., Saintonge, A., Santini, P., Grazian, A., Lutz, D., Brusa, M., Altieri, B., Andreani, P., Aussel, H., Berta, S., Bongiovanni, A., Cava, A., Cepa, J., Cimatti, A., Daddi, E., Dominguez, H., Elbaz, D., Förster Schreiber, N., Genzel, R., Gruppioni, C., Magdis, G., Maiolino, R., Magnelli, B., Nordon, R., Pérez García, A. M., Poglitsch, A., Pozzi, F., Riguccini, L., Sanchez-Portal, M., Shao, L., Sturm, E., Tacconi, L., Valtchanov, I., Wieprecht, E., and Wetzstein, M. (2011). The effect of environment on star forming galaxies at redshift. I. First insight from PACS. , 532:A145.

Postman, M., Coe, D., Benítez, Bradley, L., et al. (2012). *ApJS*, 199: 25P.

Rescigno, U., Grillo, C., Lombardi, M., Rosati, P., Caminha, G. B., Meneghetti, M., Mercurio, A., et al. (2020). , 635: A98.

Richard, J., Claeyssens, A., Lagattuta, D., Guaita, L., Bauer, F. E., Pello, R., Carton, D., Bacon, R., et al. (2021). , 646:A83.

Rodighiero, G., Daddi, E., Baronchelli, I., Cimatti, A., Renzini, A., Aussel, H., Popesso, P., Lutz, D., Andreani, P., Berta, S., Cava, A., Elbaz, D., Feltre, A., Fontana, A., Förster Schreiber, N. M., Franceschini, A., Genzel, R., Grazian, A., Gruppioni, C., Ilbert, O., Le Floch, E., Magdis, G., Magliocchetti, M., Magnelli, B., Maiolino, R., McCracken, H., Nordon, R., Poglitsch, A., Santini, P., Pozzi, F., Riguccini, L., Tacconi, L. J., Wuyts, S., and Zamorani, G. (2011). , 739(2):L40.

Schmidt, K. B., Treu, T., Brammer, G. B., Bradač, M., Wang, X., Dijkstra, M., Dressler, A., et al. (2014). , 782:L36.

Scoville, N., Aussel, H., Sheth, K., Scott, K. S., et al. (2014). *ApJ*, 783: 84.

Scoville, N., Lee, N., Vanden Bout, P., Diaz-Santos, T., Sanders, D., Darvish, B., Bongiorno, A., Casey, C. M., Murchikova, L., Koda, J., Capak, P., Vlahakis, C., Ilbert, O., Sheth, K., Morokuma-Matsui, K., Ivison, R. J., Aussel, H., Laigle, C., McCracken, H. J., Armus, L., Pope, A., Toft, S., and Masters, D. (2017). Evolution of Interstellar Medium, Star Formation, and Accretion at High Redshift. , 837(2):150.

Scoville, N., Sheth, K., Aussel, H., Vanden Bout, P., Capak, P., Bongiorno, A., Casey, C. M., Murchikova, L., Koda, J., Álvarez-Márquez, J., Lee, N., Laigle, C., McCracken, H. J., Ilbert, O., Pope, A., Sanders, D., Chu, J., Toft, S., Ivison, R. J., and Manohar, S. (2016). ISM Masses and the Star formation Law at

Z = 1 to 6: ALMA Observations of Dust Continuum in 145 Galaxies in the COSMOS Survey Field. , 820(2):83.

Scoville, N. Z. (2013). *Evolution of star formation and gas*, pages 491.

Sifón, C., Menanteau, F., Hasselfield, M., Marriage, T. A., Hughes, J. P., Barrientos, L. F., et al. (2013). , 772:25.

Solomon, P. M., Downes, D., and Radford, S. J. E. (1992). Warm Molecular Gas in the Primeval Galaxy IRAS 10214+4724. , 398:L29.

Speagle, J. S., Steinhardt, C. L., Capak, P. L., and Silverman, J. D. (2014). A Highly Consistent Framework for the Evolution of the Star-Forming "Main Sequence" from z ~0-6. , 214(2):15.

Stern, D., Jimenez, R., Verde, L., Stanford, S. A., and Kamionkowski, M. (2010). , 188:280–289.

Suzuki, T. L., Onodera, M., Kodama, T., Daddi, E., Hayashi, M., Koyama, Y., Shimakawa, R., Smail, I., Sobral, D., Tacchella, S., and Tanaka, I. (2021). Dust, Gas, and Metal Content in Star-forming Galaxies at z $\sim$ 3.3 Revealed with ALMA and Near-IR Spectroscopy. , 908(1):15.

Tacconi, L. J., Genzel, R., Saintonge, A., Combes, F., García-Burillo, S., Neri, R., Bolatto, A., Contini, T., Förster Schreiber, N. M., Lilly, S., Lutz, D., Wuyts, S., Accurso, G., Boissier, J., Boone, F., Bouché, N., Bournaud, F., Burkert, A., Carollo, M., Cooper, M., Cox, P., Feruglio, C., Freundlich, J., Herrera-Camus, R., Juneau, S., Lippa, M., Naab, T., Renzini, A., Salome, P., Sternberg, A., Tadaki, K., Übler, H., Walter, F., Weiner, B., and Weiss, A. (2018). PHIBSS: Unified Scaling Relations of Gas Depletion Time and Molecular Gas Fractions. , 853(2):179.

Treu, T., Brammer, G., Diego, J. M., Grillo, C., et al. (2016). *ApJ*, 817: 60.

Treu, T., Schmidt, K. B., Brammer, G. B., Vulcani, B., Wang, X., Bradač, M., Dijkstra, M., Dressler, A., et al. (2015). , 812:114.

van Dokkum, P. G., Whitaker, K. E., et al. (2010). *ApJ*, 709: 1018.

Villanueva, V., Ibar, E., Hughes, T. M., Lara-López, M. A., Dunne, L., Eales, S., Ivison, R. J., Aravena, M., Baes, M., Bourne, N., Cassata, P., Cooray, A., Dannerbauer, H., Davies, L. J. M., Driver, S. P., Dye, S., Furlanetto, C., Herrera-Camus, R., Maddox, S. J., Michałowski, M. J., Molina, J., Riechers, D., Sansom, A. E., Smith, M. W. L., Rodighiero, G., Valiante, E., and van der Werf, P. (2017). VALES I: the molecular gas content in star-forming dusty H-ATLAS galaxies up to z = 0.35. , 470(4):3775–3805.

Vulcani, B., Poggianti, B. M., Finn, R. A., Rudnick, G., Desai, V., and Bamford, S. (2010). Comparing the Relation Between Star Formation and Galaxy Mass in Different Environments. , 710(1):L1–L6.

Walter, F., Decarli, R., Aravena, M., Carilli, C., Bouwens, R., da Cunha, E., Daddi, E., Ivison, R. J., Riechers, D., Smail, I., Swinbank, M., Weiss, A., Anguita, T., Assef, R., Bacon, R., Bauer, F., Bell, E. F., Bertoldi, F., Chapman, S., Colina, L., Cortes, P. C., Cox, P., Dickinson, M., Elbaz, D., Gónzalez-López, J., Ibar, E., Inami, H., Infante, L., Hodge, J., Karim, A., Le Fevre, O., Magnelli, B., Neri, R., Oesch, P., Ota, K., Popping, G., Rix, H.-W., Sargent, M., Sheth, K., van der Wel, A., van der Werf, P., and Wagg, J. (2016). ALMA Spectroscopic Survey in the Hubble Ultra Deep Field: Survey Description. , 833(1):67.

Zabel, N., Davis, T. A., Smith, M. W. L., Maddox, N., Bendo, G. J., Peletier, R., Iodice, E., Venhola, A., Baes, M., Davies, J. I., de Looze, I., Gomez, H., Grossi, M., Kenney, J. D. P., Serra, P., van de Voort, F., Vlahakis, C., and Young, L. M. (2019). The ALMA Fornax Cluster Survey I: stirring and stripping of the molecular gas in cluster galaxies. , 483(2):2251–2268.